Deformation of a young salt giant: regional topography of the Red Sea Miocene evaporites

Neil C. Mitchell[1], Marco Ligi[2], Peter Feldens[3] and Christian Hübscher[4]

[1]School of Earth, Atmospheric and Enviromental Sciences, University of Manchester, Williamson Building, Oxford Road, Manchester M13 9PL, UK.

[2]ISMAR, CNR, Bologna, Italy

[3]Institute of Geosciences, Christian Albrechts University, Kiel, Germany

[4]University of Hamburg, Germany

This is an open-access pre-publication copy of an article published in Basin Research: http://dx.doi.org/10.1111/bre.12153

Keywords: Red Sea evaporites, Zeit Formation, halokinetics, salt tectonics, salt giant, seismic S-reflection.

Abstract

The deformational behaviour of "salt giants" during and shortly after their deposition is difficult to decipher in ocean margin settings where the original evaporites have been deeply buried and strongly mobilized. Here, we examine seismic reflection data from the Red Sea, where evaporites deposited until the end of the Miocene (~5.3 Ma), are generally covered by only 200-300 m of low-density sediments and where the presence of an axial spreading centre allows us to observe how they have responded to a varied configuration of underlying basement. The regional morphology of the S-reflection, representing the evaporite surface, is mapped out from seismic data from 13 cruises. The S-reflection is locally rugged and commonly angular. It is either underlain by layered reflectivity, suggestive of layered evaporite beds, or by more transparent seismic character, suggestive of massive halite. On average, the depth of the reflection on the flanks of the axial rift systematically declines from 700 to 1100 m below sea level (mbsl) going northwards from 16˚N to 23˚N. In the central Red Sea, the S-reflection has 100-200-m-deep depressions, extending towards the coasts in places. In the southern Red Sea, the S-reflection forms a surface at 300-800 mbsl that appears less disrupted. We suggest that the evaporites originally had a flat, horizontal surface at the end of the Miocene and have subsequently been distorted by isostatic effects and axial rifting, which in turn promoted evaporite flowage. Off-axis evaporite depressions correspond with flows identified with multibeam sonar. Furthermore, across-rift lows in Bouguer gravity anomalies represent valleys in the underlying basement. The off-axis evaporite depressions overlie those valleys, as would be expected if halokinetic movements were greatest where the evaporites are locally thick, leading to

deflation of the evaporite surface. The thickness of post-Miocene sediment, also mapped out as part of this procedure, confirms the generally pelagic nature of this interval and increases on average from ~250 m to 300 m from the central to the southern Red Sea, mimicking the variation in pelagic productivity observed in the present water column.

Introduction

Evaporites can be deposited in rift basins during the early stages of their transitions from continental rifting to seafloor spreading (Pautot *et al.*, 1966; Bonatti *et al.*, 1970; Evans, 1978; Rona, 1982). Many large evaporite bodies ("salt giants") lie in continental margins, such as off Brazil and Angola in the South Atlantic, where they are of commercial interest owing to their associated petroleum reserves. Because of the weak rheology of halite, young evaporite bodies containing halite potentially deform shortly after deposition, influenced by locally varying relief of underlying structure, rifting and isostasy. However, these early stages are difficult to study in old marginal deposits because they are deeply buried and hence not easily accessed or imaged seismically. The pressures and temperatures of burial also commonly cause those evaporites to be strongly mobilized (Hudec & Jackson, 2006), complicating reconstruction of their early geometries.

Reconstructions of the early structure of the Messinian evaporites in the Levant Basin in the easternmost Mediterranean suggest that the deformation of giant evaporites can start while they are depositing (e.g., Bertoni & Cartwright, 2005; Hübscher & Netzeband, 2007; Gvirtzman *et al.*, 2013; Reiche *et al.*, 2014). As summarized by Hübscher and Netzeband, (2007), loading of the lithosphere

by the evaporites there promoted basin subsidence and the resulting tilting caused the growing evaporite body to creep towards the basin center, producing internal folding and thrusting ("gravity gliding"). After re-flooding of the Mediterranean, basinward prograding Plio-Pleistocene (PP) sediment prisms squeezed the evaporites forward ("gravity spreading").

The Red Sea (Figure 1) is another region with young evaporites. In contrast to the Mediterranean, the central and southern Red Sea hosts an active spreading centre mid-way between the coasts. The spreading centre shallows by around 1 km from the central to southern Red Sea (Mitchell & Park, 2014) towards the Afar plume (Chang & van der Lee, 2011; Rooney *et al.*, 2012) in keeping with around 60˚C southward increase in mantle temperature inferred from basalt geochemical data (Haase *et al.*, 2000). In the central Red Sea, the spreading centres (the Red Sea "deeps") are marked by outcropping volcanic geomorphology and seafloor spreading anomalies, but outside the deeps the seabed morphology is smoother and magnetic anomalies are subdued, making their interpretation more ambiguous. Researchers have suggested that the underlying crust in these areas is either oceanic (Tramontini & Davies, 1969, Mitchell & Park, 2014; LaBrecque & Zitellini, 1985) or highly extended continental (Cochran, 1983; Bonatti, 1985; Ligi *et al.*, 2011; Ligi *et al.*, 2012). The nature of the off-axis crust in the southern Red Sea is also uncertain. While seafloor-spreading anomalies can be identified there up to anomaly 3 (Roeser, 1975), further lineated anomalies occurring nearer to the coasts are poorly formed for oceanic spreading anomalies, leading to varied oceanic or intruded continental interpretations (Girdler & Styles, 1974; Hall, 1989; Cochran, 1983; Mitchell *et al.*, 1992). The results of a deep-seismic refraction line near 16˚N

extending south of the Farasan Islands suggest that an oceanic crust underlies the westerly end of that line (Milkereit & Fluh, 1985; Mooney *et al.*, 1985). However, seismic refraction results from around 15°N have revealed continental crust (Egloff *et al.*, 1991). The northern Red Sea is probably floored by highly extended continental crust (Cochran, 2005; Cochran & Karner, 2007). This diversity offers the possibility for us to observe how the style of evaporite deformation reflects a varied and potentially time-varying basement structure and pattern of subsidence.

A prominent seismic reflection, called the "S" reflection, is observed throughout most of the Red Sea and has been interpreted as the top of the Miocene evaporites or Zeit Formation (Knott *et al.*, 1966; Phillips & Ross, 1970; Ross & Schlee, 1973). Examples are shown in Figure 2. For brevity, we refer to this reflection as simply "S". In the Deep Sea Drilling Project (DSDP) drilling reports (Whitmarsh *et al.*, 1974), S at Sites 225 and 228 (Figures 1 and 3) was suggested to correspond with the top of anhydrite beds marking the termination of the evaporite phase, whereas at Site 227 it was suggested to correspond with hard claystones lying up to 32 m above the evaporites. Although the stratigraphic level represented by S is somewhat uncertain, it is likely near to the top of the evaporite deposits if not their top exactly. Previously, the regional pattern of this surface has been reported only for the margins of the Red Sea, where it is commonly deep and strongly distorted by marginal sediment loading (Mitchell *et al.*, 1992).

The PP sediments overlying S in the main trough of the Red Sea (between the axial deeps and the shelves) are mostly hemipelagic and typically only 200-300 m thick (Ross & Schlee, 1973). Sedimentation rates vary only modestly

along the sea in shallow sediment cores (Figure 4). The PP sediments have similar bulk densities to halite, so there is less potential energy available to drive gravity spreading or diapirism from loading by these sediments than in more typical marginal settings (Mitchell *et al.*, 2010a).

Surveying with multibeam echosounders has revealed giant flow-like features interpreted as evaporite or salt flows (Mitchell *et al.*, 2010a; Mitchell *et al.*, 2010b; Augustin *et al.*, 2014; Feldens & Mitchell, 2015). As in the Levant Basin (Netzeband *et al.*, 2006) and Cyprus Arc (Hübscher *et al.*, 2009), the Red Sea evaporite movements appear to be driven by topographic gradients as originally suggested by Girdler and Whitmarsh (1974), but the details of the factors modulating flowage rates remain uncertain in a more quantitative sense (Feldens & Mitchell, 2015).

In this study, we accumulate information on S from seismic data collected during 13 cruises, mostly away from the margins. Seismic records originally collected on RV *Conrad* during cruise RC0911 have remained unreported in the literature, though the data are of good quality considering their age (1965) and cover the length of the basin (Figure 1). These, combined with seismic data from Italian and German cruises and legacy datasets derived from the literature and online resources, allowed the depth of S to be mapped along the whole Red Sea. Regional and local variations in the S depth can then be interpreted, as well as variations in the thickness of PP sediments overlying S. In our interpretation, widespread halokinetics (Girdler & Whitmarsh, 1974) have most strongly affected the morphology of the evaporites in the central Red Sea.

Data and methods

Sources of seismic data

The distribution of cruise tracks for which we have accumulated information on depth to S is shown in Figure 5c. The annotation in the figure key refers to RV *Glomar Challenger* (DSDP) cruise 23 (Whitmarsh, 1974), regional surveys for the Red Sea Commission (Izzeldin, 1987; 1989), RRS *Discovery* cruise 103 (Garfunkel *et al.*, 1987), RV *Chain* cruises 43 (Knott *et al.*, 1966), 61 (Phillips & Ross, 1970) and 100 (Ross & Schlee, 1973; Searle & Ross, 1975), NOs *Noroit* and *Jean Charcot* (Guennoc *et al.*, 1988), RV *Robert Conrad* cruise RC0911, RV *Poseidon* cruise P408 (Schmidt *et al.*, 2011), RV *Pelagia* cruise 64PE350 (Schmidt *et al.*, 2013), MVs *Salernum* cruise MR79 and *Bannock* cruise MR83 (Bonatti *et al.*, 1984) and RV *Urania* cruise RS05 (Mitchell *et al.*, 2010a; Ligi *et al.*, 2011; Ligi *et al.*, 2012). For general corroboration, the top of the evaporites have also been reached by drilling at the sites indicated in Figure 1.

Character of the S reflection and associated strata

The selection of seismic data in Figure 2 was collected on RV *Conrad* during cruise RC0911 along the red lines marked in Figure 1 and illustrates many of the features reported in prior publications. S is a prominent reflection commonly observed lying at 200-300 ms two-way time below the seabed reflection, except near the coasts where it can deepen steeply landward (e.g., Figure 2a). S is either a sharp reflection of less than 40 ms two-way time with limited reflectivity below it or a prominent reflection underlain by layered reflectivity, extending for example to 150 ms in Figure 2b. In the latter case, the choice of S in parts of the data can be subjective, though usually a prominent reflection characteristic of S is distinguishable within the layered reflectivity.

Seismic data collected on RV *Urania* in 2005 were intended for deeper imaging so they do not have much high frequency content, but nevertheless the examples processed to enhance high frequencies shown in Figure 6 clearly reveal the S reflection.

Mapping the depth of the S reflection

The two-way times to the S and seabed reflections were recorded from the data (Figure 5c). A minority of the data were digital (collected on vessels *Urania, Poseidon* and *Pelagia*), allowing the reflections to be mapped using commercial seismic interpretation software. Scanned paper records of RV *Conrad* RC0911, RRS *Discovery* 103 and RV *Glomar Challenger* (DSDP) cruise 23 were used to record two-way times and survey times. The scanned images of seismic data from the RV *Chain* cruises were difficult to interpret and commonly lacked survey time marks. We chose instead to digitize from the published interpretational cross-sections (Knott *et al.*, 1966; Phillips & Ross, 1970; Ross & Schlee, 1973; Searle & Ross, 1975), which are presumed to be more reliable as they had been derived directly from the original paper records. Upon merging those data with navigation from their associated maps, we discovered some minor positional discrepancies between the seabed reflection and modern bathymetry compilations (Becker *et al.*, 2009). We reconciled those discrepancies so that geomorphological features in the two datasets matched by applying shifts in longitude (all $\leq 0.15^{\circ}$) to the *Chain* data. This also greatly reduced S and seabed depth errors at crossing lines.

Two-way times to the seabed were converted to water depths using a mean velocity of 1538 m s^{-1} expected for a typical Red Sea salinity of 40 ppt and

temperature of 21˚C (Sofianos & Johns, 2007) with the empirical equations of Mackenzie (1981). Depths to S and PP sediment thicknesses were computing assuming a sediment P-wave velocity of 1900 m s^{-1} based on measurements made on samples recovered during DSDP Leg 23 (Whitmarsh *et al.*, 1974) summarized in Figure ES2. Seismic refraction experiments typically do not resolve the PP sediment velocity well, but 1900 m s^{-1} is centred within the range of most values (1800-2000 m s^{-1}) reported from expanding spread experiments in the northern Red Sea (Gaulier *et al.*, 1988) and is comparable with results of earlier refraction experiments (Drake & Girdler, 1964). A multichannel seismic velocity analysis presented by Izzeldin (1982) suggests locally 2038 m s^{-1} for this layer, although this was for data located nearer to the Sudanese coast where a greater terrigenous sediment component might be expected. Velocity uncertainty (a variation of 100 m s^{-1} or more in velocity is possible) affects the PP thickness and depth to S, but, as the PP sediments are uniform and only 200-300 ms thick generally, these uncertainties are minor. An exception is near to the coasts where S deepens and overlying thick sediments may be more terrigenous and thus of higher velocity.

Depth to S and thickness of overlying sediment were binned over 0.1˚ of latitude and longitude and subsequently interpolated onto a grid with a surface-fitting program (Smith & Wessel, 1990). The data are shown in Figures 5 and 7 with areas more than 0.15˚ of latitude or longitude from vessel tracks masked out. The procedure led to erroneous interpolation across the floors of the deeps, which are known to be almost bare of sediment where volcanic geomorphology is observed. These areas were therefore also masked out using the interpretation of Augustin et al. (2014). In Figure 7, the depth of S is shown

along with (inset to the figure) halokinetic flowage structures interpreted from multibeam data by Augustin et al. (2014). The texture in the main panel of Figure 7 is provided by artificial shading of the multibeam bathymetry from the NE (areas without texture are typically not covered by these data).

For the purpose of studying regional trends, the depth and PP thickness data were binned over 0.015˚ and those binned data separated into corridors 30 to 100 km from the spreading axis on each flank as marked in Figures 5a, 5b and ES3. To highlight the along-axis trends, the results are shown projected along-rift in Figure 8, along with values averaged every 200 km (solid black circles).

The pattern of basement topography from Bouguer gravity anomalies

The Red Sea segment of the free air gravity field derived from satellite altimetry by David Sandwell and others (Sandwell & Smith, 1997) was studied by Mitchell and Park (2014), who identified gravity anomaly lows in version 21 that cross the Red Sea roughly parallel with the plate spreading direction. Gravity anomalies represent the combined effect of density variations within the crust and upper mantle, and of topography of the Moho and crust-evaporite interfaces, as well as seabed topography. However, away from the deeps, seabed topography in the Red Sea is subdued and free air gravity anomalies were found to correlate with basement depths from refraction experiments, so local gravity variations at least partly follow the topography of basement beneath the evaporites. The gravity anomaly lows crossing the Red Sea were therefore claimed to correspond with valleys in the underlying basement (Mitchell & Park, 2014).

To demonstrate further that the pattern is not an artifact of bathymetry, we have computed a map of gravity anomalies corrected for bathymetry variations (i.e., marine Bouguer anomalies; Figure 9b). The calculations were carried out on version 22 of the Sandwell and Smith (1997) free air anomaly grid. The 1.13 g cm^{-3} density contrast used here corresponds to halite (2.16 g cm^{-3}) with seawater (1.03 g cm^{-3}). As the PP sediments are pelagic and somewhat uniform in thickness as shown later, an evaporite-seawater (rather than PP sediment-seawater) density contrast is the appropriate one to use to remove the seabed effect. In addition, the average density of the PP sediments at the DSDP sites is similar to that of halite (Mitchell *et al.*, 2010a) (Figure ES2) so only minor errors are likely to arise from PP thickness variations. A further map computed using a density representing layered evaporites (2.5 g cm^{-3}) shows similar features (Figure ES4).

The high values along the centre of the Red Sea in Figure 9b result mainly from dense mantle rocks elevated under the spreading axis or a transition to continental crust (Ligi *et al.*, 2012). Sub-orthogonal to that axial trend, a series of depressions cross the Red Sea NE to SW, parallel with the Nubia-Arabia plate spreading direction (Chu & Gordon, 1998). Although we cannot rule out a contribution from crustal or upper mantle density variations, these features are geometrically consistent with elongated basement depressions crossing the Red Sea, such as oceanic spreading fracture zones (Mitchell & Park, 2014) or accommodation zones between fault blocks in highly extended continental crust.

Observations and interpretations

Features in seismic data and character of S

Evaporite character

S tends to have greater relief where it is underlain by transparent seismic character and is flatter lying where underlain by layered reflectivity (Figure 2). Izzeldin (1987) interpreted layered reflectivity below S in his data from the central Red Sea as stratified evaporites (alternating halite, anhydrite and shale beds, as found in the DSDP cores (Whitmarsh *et al.*, 1974); Figure 3) and the more transparent reflection character as massive halite. We similarly attribute the transparent and layered reflectivity immediately below S in the seismic data in Figures 2 and 6 to these different evaporite deposit types. The greater relief of the sharp S would then be consistent with diapirs (Ross & Schlee, 1973), whereas the layered evaporite is a composite material containing stronger lithologies that are apparently less easily deformed and can be expected to be denser than halite because of their anhydrite components (Wheildon *et al.*, 1974).

Tectonic growth structures

In parts of the *Conrad* seismic dataset, the reflections beneath S vary in dip with respect to both S and the modern seabed reflection. Commonly, as in Figure 2a, reflections below S are steeper than S. In Figure 6a, where located by ellipses, reflections beneath S are discordant with S. In particular, around shot point (SP) 500, a small syncline shows discordant upper Miocene reflections and some discordant PP reflections above S, while the upper PP reflections are concordant with each other and with the seabed reflection. Varied dips of evaporite reflections can also be observed at SP 200 in Figure 6b. Overlying S there, the PP strata appear disrupted, suggesting continuing movement

associated with this anticline, or the results of fluid expulsion. The small syncline at SP 320 in Fig. 6b is almost filled with PP sediment (this feature corresponds in multibeam sonar data to a small trough running to the north, oblique to the wall of the adjacent deep (Mitchell *et al.*, 2010a)). The uppermost third of the PP in the syncline is roughly flat lying, whereas the lowermost two thirds are more conformable with S.

We suggest that these features represent tectonic growth structures and that the evaporites were mobile during the Miocene evaporite stage. Ehrhardt and Hübscher (2015) similarly interpreted tectonic growth structures observed in their data in the northern Red Sea as the result of syn-depositional salt tectonics. Changing dips of reflections in the layered evaporite with depth suggest that this deformation occurred in an unsteady manner (e.g., around SP 180-220 in Figure 6b).

Unconformities

In Figure 6b (SP 360 to 460), a gently dipping angular unconformity is marked, where reflections immediately below S dip to the NW in the section. A more curvilinear unconformity can be observed over the anticline at SP 200 in that figure. Further unconformities at S were reported nearer to the Sudanese coast (Izzeldin, 1987; Bunter & Abdel Magid, 1989).

Although a tectonic explanation for these unconformities (slump faults) cannot be ruled out entirely, faults are considered unlikely because the unconformities cut cleanly across strata rather than following weak layers and there is no evidence for the consequential slump deposits. Furthermore, the marginal unconformities (Izzeldin, 1987; Bunter & Abdel Magid, 1989) would be

difficult to explain in terms of slope failure, as slope failure is unlikely to be widespread and many of these unconformities are horizontal (Izzeldin, 1987). Fluvial erosion also cannot be ruled out entirely, but there are no obvious thalwegs, interfluves or fluvial terraces in the seismic data (e.g., Figure 6b). Subaerial exposure to rainfall and dissolution of soluble evaporite minerals might have led to a widespread unconformity if these areas were exposed above sea level.

Similar features in the Mediterranean have influenced our interpretation. Bache et al. (2009) mapped rough and smooth unconformities at the top of Miocene sediments in the Gulf of Lions. The rough unconformities contain dendritic fluvial-like paleovalleys, whereas the smooth unconformities lie deeper and seaward of the rough unconformities. Bache et al. (2009) interpreted the smooth unconformities as caused by surf erosion during transgression at the end of the Messinian Salinity Crisis and rough unconformities as produced by subaerial erosion. The curvilinear but generally smooth morphology of the central Red Sea unconformities such as those in Figure 6b and those of Izzeldin (1987) seem to us more like the smooth unconformities of Bache et al. (2009) than their rough unconformities. We therefore suggest that the unconformity in Figure 6b was created by surf erosion primarily, and possibly freshwater dissolution, with its local relief developed later by halokinetic deformation.

Topography of the S reflection

In Figure 5a, S generally deepens both towards extreme values at the coasts where it is depressed by terrigenous sediments (Mitchell et al., 1992) and towards the axis of the Red Sea, where it falls by typically ~1000 m. Away from

those central deep areas and the coasts, S is rugged though with flatter areas between depressions. In the northern Red Sea, S forms a broad depression elongated parallel with the NW trend of the Red Sea. In Figure 8, ignoring the local spikes upwards (which are associated with diapirs), flatter areas occur at 300-800 mbsl from 17˚-18˚N, deepening in the central Red Sea (22˚-23˚N) to 800-1200 mbsl. The mean elevations also decline northwards from ~700 mbsl at 17˚-18˚N to ~1100 mbsl at 22˚-23.5˚N. Given the greater consistency of the shallower S depths along the Red Sea (red areas in Figure 5a) compared with areas of deeper S depths, these are suggested to represent the original evaporite top and deeper areas (yellow and green in Figure 5a) are where the evaporite has declined because of flowage towards the spreading rift axis.

In Figure 7, many of the depressions of S away from the axis can be associated with flowage structures observed in the multibeam data. For example, around Atlantis II and Discovery Deeps, flows of evaporites in the multibeam data lie downslope from depressions L2 and L9 and towards the deeps. The inter-trough zone (ITZ) north of Thetis Deep is flanked by L3 and L6. The flows in the northeast walls of Hadarba and Hatiba deeps lie immediately southwest of L7 and L8. The ITZ between Erba and Poseidon Deeps is associated with L11 on the Arabian side, though slightly offset, and with minor depression L1 on the African side. Where the axis is not greatly invaded by evaporite flows, the axial valley floor tends to be wider, with volcanic geomorphology observed in the multibeam data (Augustin *et al.*, 2014). These evaporite-free parts of the axis are associated laterally with highs in S, where the reflection commonly lies shallower than 1100 mbsl.

In Figure 9c, the Bouguer gravity contours of Figure 9b are overlain on the map of S depth to aid comparison. Several of the cross-axis valleys in the gravity anomalies coincide with depressions in S. The Nereus-Thetis ITZ (L3 and L6), for example, is associated with such a valley. L9 is a broad depression of S lying at ~1200 mbsl and extending to the coast near Jeddah, with deeper lows in its north and south sides. The gravity data suggest there are two cross-axis valleys here, underlying the two narrow deeper lows at the N and S sides of L9. L1 and L11 are also associated with a deep cross-axis low in the gravity data.

Where the axial Bouguer anomaly is high and less disrupted by cross-axis valleys, S on the adjacent flanks tends to be elevated and less disrupted. This is striking south of 20˚ 30'N, but also occurs at 21˚N, 22˚N and 23˚10'N (Aswad, Hatiba and Nereus Deeps). A seismic reflection line of Izzeldin (1987) crossing Nereus Deep shows that the basement is elevated on both sides of the deep there.

The S-reflection morphology, coupled with flowage structures in the multibeam data and depressions in the Bouguer anomalies, suggest that the evaporites have been flowing towards the rift axis most extensively where the basement beneath the evaporites is deeper. Flowage rates may be larger over valleys simply because net discharge will be larger for a given shear strain rate (for a viscous flow coupled at its base, the flow discharge and velocity at its surface are obtained by integrating the strain rate over the vertical extent of the flow (Turcotte & Schubert, 1982)). However, rock deformation laws, such as those for halite pressure solution creep (Spiers *et al.*, 1990), suggest that strain rates should be larger where the rock temperature is higher (Feldens & Mitchell, 2015), which can also be expected where the evaporite is thicker.

Some isolated locally elevated gravity anomalies may represent buried seamounts. These potentially retard evaporite flowage. One small potential seamount was identified previously east of Thetis Deep (Mitchell & Park, 2014). The gravity high east of Atlantis II Deep (Figure 9b) appears to have forced the overlying collapse structure (L9 between H11 and H12 in Figure 9a) to divide into two sets of flows entering the spreading centre.

PP sediments overlying the S reflection

Within the PP sediments overlying S in Figure 2, reflectivity is strong near to the seabed but becomes weaker (transparent) towards S. This character is typical of the PP in the central and southern Red Sea. As the sea is connected to the Indian Ocean by a shallow sill, exchange with the Indian Ocean becomes restricted during glacial low-stands of sea level, leading to high salinity in the Red Sea. Layers of inorganic aragonite were consequently deposited during the late Pleistocene glacial low-stands (Almogi-Labin *et al.*, 1986; Hemleben et al., 1996). These are likely more rigid than intervening sediment and are probably the origin of the upper PP reflectivity. In the earlier Pleistocene and Pliocene, sea level was generally higher and fluctuated less (Elderfield *et al.*, 2012); smaller fluctuations in salinity and associated more uniform pelagic physical properties may explain the more transparent lower PP seismic reflectivity.

In contrast, the data in Figure 6b show a layered lower PP. Two further examples of data showing lateral changes from layered and transparent lower PP from the northern Red Sea (Figure 1) are shown in Figures ES1a and ES1b. In shallow cores, the Red Sea PP is less dominated by biogenic material than are pelagic sediments in the some open oceans above the carbonate lysocline

(Stoffers & Ross, 1974; Locke & Thunell, 1988). For example, $CaCO_3$ concentration is only ~50% on average for core KL11 (Figure 1) (Almogi-Labin *et al.*, 1996) with the remainder comprising terrigenous quartz, feldspar and clay minerals (Stoffers & Ross, 1974; Hofmann *et al.*, 1998). Most of this non-pelagic component is wind-blown dust (Roberts *et al.*, 2011). Thus, areas where the lower PP is reflective may represent variability of dust input or some fluvially-sourced terrigenous sediment.

The thickness of PP sediments can vary locally by more than a factor of two in Figure 6b. In the Atlantis II Deep area, depression L9 is associated with thicker PP sediments (Fig. 5b) but otherwise these variations are not obviously connected with the topography of S, i.e., depressions of S are not associated with preferentially thicker PP sediments as would be the case if there had been generally gravity-driven sediment transport. In some parts of the data, the sediments are flat lying (typical of turbidites), such as at SP320 in Figure 6b (also see Figure ES1a from farther north). However, more usually the PP drapes the underlying S reflection, varying from almost perfectly paralleling S to forming a more attenuated version of the topography of S typical of pelagic sediments.

In the regional pattern (Figure 5b), the PP thins (to <200 m) both north of 19˚N and towards the axis of the Red Sea. Where we have seismic data collected close to the coasts, the PP thickness can exceed 500 m. The average PP thickness of the ridge flanks, sampled in the same manner as the S depths (Figure 8), declines from 300 m to 240-250 m from 17˚-19˚ to 20˚-21˚N, before increasing again north of 23˚N (the decline is better revealed in an along-rift profile of the average thicknesses in Figure ES5). The PP thickness declines by >100 m towards the axis of the Red Sea in areas north of 19˚N.

Away from the deep marginal deposits, the thinning of the PP away from the coasts in the central and northern Red Sea probably arises from the fallout of aeolian particles (Stein *et al.*, 2007; Roberts *et al.*, 2011; Palchan *et al.*, 2013). If 50% of the sediment is biogenic and the input of biogenic particles does not vary with distance from the coasts, a 100 m increase in PP thickness towards the coasts from 200 m near the axis would require a doubling of the terrigenous flux. In the DSDP cores, terrigenous components were found to increase with core depth into the Pliocene (Stoffers & Ross, 1974) so the particle input responsible for this variation may have been different from the Late Pleistocene where most of the work on sediment cores has been carried out.

Explaining the thickening of the PP into the southern Red Sea is difficult without more extensive core information. Minor volcanic particles recovered at DSDP Site 229 (Figure 1) (Stoffers & Ross, 1974) suggest that volcanism in the southern Red Sea may have contributed to the PP thickness trend, though total non-biogenic components were only 10% at the site (Whitmarsh *et al.*, 1974). The modern Red Sea is nutrient-limited and intrusion of Indian Ocean waters through the Bab el Mandab Strait causes high productivity of phytoplankton (Bouilloux *et al.*, 2013). Measurements of Petzold (1986) reproduced in Pfannkuche (1993) show surface primary production abruptly increasing southwards from around 200 to 2200 mgC m^{-2} d^{-1} from 16˚ to 15˚N. This is more abrupt and occurs south of the change in PP thickness in Figures 5b, though other measures of biological activity such as meiofauna densities and chlorophyll (Petzold, 1986) extend farther northwards into the central Red Sea around 20˚N. Much of the regional trend in PP thickness could therefore have arisen from varied accumulation of biogenic particles.

Discussion

The regional northward deepening trend in S depth (Figure 8) is curious if the evaporites were supplied from the Mediterranean as suggested based on the Mediterranean provenance of calcareous nannofossils identified by Boudreaux (1974) within the intercalated black shales of the evaporites drilled at DSDP Sites 225 and 227 (Figure 1) (Orszag-Sperber *et al.*, 1998) and Mediterranean fauna in marginal commercial wells (e.g., (Bunter & Abdel Magid, 1989; Hughes, 2014). Studies of the commercial wells have concluded that much of the middle Miocene evaporites were deposited in deep water (Crossley *et al.*, 1992; Hughes & Beydoun, 1992). Their regional top surface need not necessarily therefore have been horizontal at the time of deposition. However, Hughes and Beydoun (1992) interpreted a transition to shallow water precipitation in the Upper Miocene (Zeit Formation), with interbedded shallow- to marginal-marine clastics. Stoffers and Kühn (1974) interpreted the evaporites at DSDP sites 225, 227 and 228, where they comprise alternating anhydrite, halite and shale (Figure 3), as deposited in sabka or shallow water environments. Orszag-Sperber et al. (1998) summarizing the literature available also concluded that a shallow water depositional environment could explain the layered evaporites of the Upper Miocene Zeit Formation, although they remarked that the precise water depth is difficult to estimate.

If the reflective character of evaporites is interpreted similarly as arising from alternating anhydrite, halite and shale deposited originally in shallow water (Izzeldin, 1987), the occurrence of reflective character at many locations along the Red Sea (Izzeldin, 1987; Ehrhardt *et al.*, 2005; Ehrhardt & Hübscher, 2015)

(Figures 2, 6 and ES3) suggests that shallow water covered much of the basin at the end of the Miocene. We suspect this water body was continuous throughout the Red Sea rather than forming isolated bodies in sub-basins of different elevation because we have been unable to find evidence for paleo-barriers in the seismic data studied. For example, at ~20˚ 30' N there is an important transition in S depth (Figure 9) that was crossed by the seismic data collected during the DSDP expedition (Whitmarsh, 1974). Those data show only a gradual decline in S, not an obvious barrier or step.

The unconformity in Figure 6b presently lies at a lower elevation than many parts of the seismic data we have viewed where evaporite layered reflectivity is conformable with S (e.g., Figure 2), implying a lack of erosion (the S depths at the locations marked by red circles in Figures 2b and 6b are shown in Figure 8). If, as we suggest, this unconformity was produced by surf erosion, its lower elevation implies that the movement of the evaporites has changed the order of the S elevations, as the unconformities should have originally lain above the areas of S that were not eroded and thus continually below surf level. The unconformities, paleontologic and seismic evidence suggest that the evaporites formed a more nearly horizontal surface at the end of the Miocene and those in the central Red Sea have deepened on average relative to those in the south.

Isostatic adjustments and the regional variation in S depth

We explore here possible contributions to the regional trend in S depth from isostasy. Tectonic subsidence is difficult to predict because of the uncertainty in the type of crust in the central and southern Red Sea mentioned earlier and in its age even where it is oceanic. Nevertheless, reconstructing the

surface assuming that the crust is wholly oceanic formed at a central spreading centre provides a likely upper bound on the tectonic subsidence (if the crust is instead extended continental crust, the subsidence calculation neglects the thermal insulating effect that a thicker mantle lithosphere provides (McKenzie, 1978)). As the evaporites cannot have been deposited above sea level, they provide a constraint on the subsidence in the following discussions. Furthermore, the regional trend in the reconstructed elevations of the evaporites can also be compared with the pattern of flowage inferred earlier.

The calculation involves a simple Airy adjustment for isostatic effects of water and PP sediment loading, and lithospheric thermal subsidence. Only a simple Airy adjustment is justified given the poor constraints on lithospheric rigidity, but S depths are nevertheless averaged over scales larger than the length-scale over which loads are likely to deform flexurally the surrounding lithosphere, <70 km for oceanic lithosphere of slow-spreading ridges with effective elastic thicknesses <13 km (Cochran, 1979; Louden & Forsyth, 1982). The Airy isostatic change in lithosphere elevation h resulting from loading by a layer of thickness H and density ρ is $H\rho/\rho_m$, where ρ_m is the density of the displaced mantle rocks. We use an upper mantle density ρ_m=3.15 g cm^{-3} from Makris et al. (1991), compatible with low seismic velocities beneath the southern Red Sea.

Successive adjustments are shown by the series of solid lines in Figure 8. An adjustment was made first for the present water layer using the mean depth in each interval and with a water density of 1.03 g cm^{-3}. An adjustment was then made for PP sediment loading using their mean thicknesses and a sediment wet

bulk density of 1.95 g cm^{-3} (based on DSDP sample measurements of Wheildon et al. (1974) in Figure ES2).

Despite the evaporites reaching several kilometres in thickness (Izzeldin, 1987), we make no allowance for their thermal insulating effect on the lithosphere given their high conductivities of ~5 W m^{-1} K^{-1} (Wheildon *et al.*, 1974), which are slightly above ~4 W m^{-1} K^{-1} conductivity of mantle rocks (Turcotte & Schubert, 1982). Although the central Red Sea has lineated magnetic anomalies (Izzeldin, 1987), they are not interpretable reliably beyond Chron 2A typically (Chu & Gordon, 1998). Anomalies of the adjacent Arabia-Somalia plate boundary in the Gulf of Aden show that spreading rates at 14˚N, 52˚E decreased from ~30 mm yr^{-1} at 15-17.5 Ma to nearer 20 mm yr^{-1} at 10 Ma and then remained constant to the present (Fournier *et al.*, 2010). Geological evidence summarized by Bosworth et al. (2005) suggests that the Aqaba-Levant transform boundary began accommodating Arabia plate motion at about 12-14 Ma, leading to a change in direction of Arabia-Nubia motion. Thus, a steady Arabia-Nubia motion after 10 Ma is suspected and a faster rate before then. To produce a lithospheric age model, we used the Chu and Gordon (1998) rotation pole and rate for Chron 2A (3.2 Ma) to predict earlier seafloor isochrons. If the Red Sea is floored by oceanic crust, the Chu and Gordon (1998) rotation pole will lead to over-estimated crustal age prior to 10 Ma, but the subsidence calculations are insensitive to these errors as subsidence rates are fastest on younger seafloor.

The mapped location of the axis (dashed line in Figure ES3) was rotated in increments of 1 m.y. to produce a grid of seafloor model age. The seafloor age under the interpreted S reflection locations (Figure ES3) was then sampled from this grid (though restricted to 5.3 Ma where data lay on seafloor younger than

5.3 Ma). The mean age of the data corresponding to the average S reflection depths was then computed. This age *a* (Ma) was then used to estimate the lithospheric subsidence since 5.3 Ma from half-space cooling for terrain older than 5.3 Ma using:

$$h = B\,(a^{0.5}-(a-5.3)^{0.5}) \quad (1)$$

The subsidence rate B was varied from 366 to 492 m m.y.$^{-0.5}$ going from north to south from the oceanic subsidence relations of Marty and Cazenave (1989, their Case 1). This variation accounts for axial depth also varying from north to south as shown in Mitchell and Park (2014), with a faster subsidence rate towards the south arising from a hotter upper mantle towards the Afar plume (Haase *et al.*, 2000; Chang & van der Lee, 2011; Rooney *et al.*, 2012), which leads to greater vertical temperature gradients and hence faster lithospheric heat losses.

Results of isostatic adjustments and their assessment

The results shown in Figure 8 reveal a few interesting trends. The isostatic changes since the end of the Miocene are clearly over-predicted south of 20°N as evaporites cannot have been deposited above global ocean level. Uncertainties in the analysis above may explain some of this over-prediction. The dispersion in the B values of Marty and Cazenave (1989) would allow B to be 50 m m.y.$^{-0.5}$ smaller (corrected mean elevations would be ~70 m lower). A 3.3 g cm^{-3} mantle density would change the PP sediment and water loading corrections by 10 m.

Our use of a model based on mantle half-space cooling (Marty & Cazenave, 1989) ignores some time-varying effects that can occur at ridges near plumes, such as from pulsing of the plume, leading to temporally varying mantle

temperature and crustal thickness (Vogt, 1979; Cannat *et al.*, 1999; Ito, 2001). Magmatic under-plating (Tiberi *et al.*, 2005) cannot be ruled out, though seems unlikely to underlie most of the data studied (Figure 5c) because there are no volcanic islands or change in incidence of isolated features likely to be seamounts in gravity data north of Farasan Islands (Figure 9b).

Almalki et al. (2014) described normal faults in the Farasan Islands, which are oriented sub-parallel with the adjacent spreading centre. They imply that some extension occurred after the Miocene on the flanks of the ridge. However, identified C2A magnetic anomalies north of 18˚N are well fit with a plate model with a single pole of rotation (Chu & Gordon, 1998), so off-axis extension by fault movements or dyke intrusions is unlikely to have been sufficient to explain the 18˚-19˚N reconstruction above sea level in Figure 8.

The C2A anomalies south of 18˚N are also explainable by extension across the Danakil Depression (Chu & Gordon, 1998). Anomaly 3 identified by Roeser (1975) at 17˚N provides a further constraint. His model shows that the peaks of magnetic anomaly 3 have the same distance across axis as the outer edge of chron 3n in the crustal magnetisation. That distance is 81 km, whereas the corresponding separation predicted using the Chu and Gordon rotation pole and rate for Nubia-Arabia is 85 km, so there is a modest discrepancy, though not a major one and it would seem to be explained by the involvement of the Danakil tectonic block at about 18˚N (Chu & Gordon, 1998). On balance, we prefer a combination of the uncertainties mentioned above, time-varying plume behavior and the presence of some non-oceanic crust to explain this discrepancy.

Around half of the regional northwards-deepening trend is explained by the water and PP sediment loading, which account for 147 m of the variation

from 17˚ to 23˚N. Interestingly, the reconstructed evaporite surface at 23˚N in Figure 8 including tectonic subsidence is only 83 m shallower than the average of the values between 17˚ and 19˚N with only water and PP loading removed. As the tectonic subsidence is an upper bound, the tectonic subsidence at 17˚-19˚N would need to be only 83 m to explain this if the evaporite had a continuous and horizontal surface at the end of the Miocene. If subsidence were purely thermal, such a small amount of subsidence seems unlikely so close to the Afar plume as explained earlier.

South of the Poseidon-Erba ITZ at 20.5˚N, the flowage of evaporites has not covered the spreading centre anywhere fully and S has a more nearly uniform elevation, at least on the Arabian flank, compared with that in the central Red Sea. It seems most likely therefore that the regional trend is a result of widespread but heterogeneous flowage in the central Red Sea, which has depressed the evaporite surface, while that in the southern Red Sea has been depressed by a lesser amount. Furthermore, if the evaporites have been strongly depressed in the south by flowage also, there would a more difficult problem of tectonic subsidence to explain there.

In conclusion, the evaporite surface was probably a continuous horizontal or nearly horizontal surface at the end of the Miocene. The isostatic calculations suggest that the surface lay closer to modern sea level and, as the upper Miocene evaporites were deposited in shallow water, this implies that the sea surface would also have been closer to global ocean level. Only a modest persistent drawdown (perhaps a few hundred metres at most and more likely near 200 m) would be compatible with the morphology of the margins of the Red Sea, which do not contain rias of the type associated with the Messinian drawdown in the

Mediterranean (Cornée *et al.*, 2014). Arabian stream profiles in Wilson et al. (2014) do not show any lower knickzones that could be evidence for Miocene rejuvination. In some areas in the central Red Sea, evaporites eroded by surf suggest that their surface was slightly higher in elevation than that in the south. Subsequently, halokinetics have deepened the central Red Sea evaporite surface by around 200 m more than the surface in the south, consistent with the morphologic evidence for greater flowage in the central Red Sea.

Relationship between the topography of S and crustal structure

Augustin et al. (2014) suggested that the volume of evaporites in each inter-trough zone (ITZ) is comparable to the volume of missing material represented by the depressions adjacent to each ITZ. This would suggest that continuous evaporite coverage over the ITZs results from evaporites in off-axis areas having flowed onto the spreading centre in those areas. However, this was based on topographic analysis using multibeam sonar data; seismic data (Tramontini & Davies, 1969; Izzeldin, 1989) in contrast suggest that the basement beneath the evaporites in ITZs is depressed, so the evaporite volumes in ITZs are larger than the volumes of the depressions. Nevertheless, evidence of tectonic growth structures in the layered evaporites shown here and elsewhere (Ehrhardt & Hübscher, 2015) suggests that the evaporites were mobile during their deposition. Evaporites may have therefore continued depositing within the depressions as they formed, reducing the depression volumes. If the ITZ and adjacent depression volumes do not correspond with each other, this does not ultimately negate the idea that the ridge axis is continuous along the central Red Sea but only obscured by evaporite flows (Augustin *et al.*, 2014).

Mitchell and Park (2014) compared depths to basement recorded in earlier seismic refraction experiments (Tramontini & Davies, 1969) with the surface geomorphology in multibeam sonar data around Thetis Deep. Those comparisons suggest that gaps or depressions in basement there allow flowage to occur into the axial valley. The broader comparison made here with the Bouguer anomalies (Figure 9b) suggests that this occurs more generally. The cross-axis basement valleys in the central Red Sea and lack of such valleys south of 20˚N in gravity anomalies have been interpreted as representing different styles of oceanic crust characteristic of slow-spreading ridges, with fracture zones in the former and a lack of fracture zones, or even axis-parallel structures in the latter, closer to the Afar plume (Mitchell & Park, 2014; Mitchell, 2015). If correct, then there is a relationship between crustal structure, the pattern of flowage and ultimately the pattern of ITZs and deeps in the central-southern Red Sea.

These observations may also be relevant to the evolution of the more marginal structures. Although the marginal evaporites are depressed by loading by terrigenous sediments, the evaporite movement towards the axis also facilitates the extension in the more marginal areas by reducing lateral constraint there. We suspect this is the case for the depression adjacent to Jeddah (Figure 2a), where a broad depression of S relates to flow into Atlantis II and adjacent deeps.

Conclusions

Regional variations in depth of the S reflection have been mapped out throughout much of the deep waters of the Red Sea. Aside from diapirs, the

upper levels of the S reflection consistently lie shallower than 1100 mbsl. In the northern Red Sea, S forms a 300-m deep depression aligned with the rift. In the central Red Sea, S is strongly disrupted by depressions, which can be associated with flowage structures observed in multibeam sonar data. Furthermore, these depressions overlie basement valleys suggested by Bouguer gravity lows, so flowage has occurred preferentially where the evaporites are thickest and less constrained by basement topography. More extensive flow could be a result simply of flow thickness (discharge of a flow of given strain rate will larger if the flow is deeper) and/or because of higher temperatures affecting strain rates.

The regional average elevation of the S reflection on the flanks of the spreading centre declines from 700 mbsl at 17˚-18˚N to 1100 mbsl at 23˚N. Simple isostatic adjustments were made to these depths for the effects of loading by the water column and Plio-Pleistocene sediments. A more speculative depth change caused by lithospheric cooling was made assuming the crust of the Red Sea is entirely oceanic. As this likely over-estimates the subsidence if the crust is instead continental, it generally provides an upper bound on the change since the end of the Miocene. Nevertheless, it suggests that the evaporite surface lay much closer to the global ocean level at that time. Although the regional trend could potentially be explained by differential lithospheric subsidence (if the southern Red Sea were continental while the central Red Sea were oceanic), we suspect instead that the evaporite flowage has reduced elevations of S in the central Red Sea substantially. An unconformity in the central Red Sea provides further support for this. If, as we suggest, it was created by surf erosion, the greater depth of this unconformity compared with areas where S in the southern Red Sea

has apparently not been eroded implies that the unconformity has subsided below those areas since the erosion phase.

The thickness of Plio-Pleistocene sediments overlying S has also been mapped out. The PP sediments are thicker in the south, possibly a result of greater pelagic productivity influenced by intrusions of Indian Ocean water, as occurs in the modern Red Sea. Some locally thick deposits occur (such as east of Atlantis II Deep), though otherwise they only vary modestly in thickness with latitude, forming a typically 200-300 m thick deposit.

Acknowledgements

We are grateful for Rose Anne Weissel for help in locating and scanning the RV *Robert Conrad* data used in this study. Nico Augustin kindly provided us with a copy of his morphological interpretation (Augustin *et al.*, 2014) and discussed the results of our analysis with us. Permissions of the governments of Egypt, Sudan and Saudi Arabia to carry out the surveys on RVs *Urania, Poseidon* and *Pelagia* are gratefully acknowledged. The *Urania* cruise was funded by the Consiglio Nazionale delle Ricerche under project LEC-EMA21F of the European Science Foundation programme EUROMARGINS (contract ERAS-CT-2003-980409 of the European Commission, DG Research FP6). The *Poseidon* and *Pelagia* cruises were part of the Jeddah Transect Project, a collaboration between King Abdulaziz University and Helmholtz-Center for Ocean Research GEOMAR Kiel funded by King Abdulaziz University (KAU) Jeddah, Saudi Arabia, under grant No. T-065/430-DSR. We thank two anyonymous reviewers, Tadeu Reis and editor Cindy Ebinger for helpful comments. ML acknowledges supporting

grant PRIN 20125JKANY_002. Figures in this article were created with the "GMT" software system (Wessel & Smith, 1991).

Conflict of interest

No conflict of interest declared.

References

ALMALKI, K.A., BETTS, R.G. & AILLERES, L. (2014) Episodic Sea-Floor Spreading in the Southern Red Sea. *Tectonophys.*, **617,** 140-149.

ALMOGI-LABIN, A., LUZ, B. & DUPLESSY, J.C. (1986) Quaternary Paleo-Oceanography, Pteropod Preservation and Stable-Isotope Record of the Red Sea. *Palaeogeog., Palaeoclim. Palaeoecol.*, **57,** 195-211.

ALMOGI-LABIN, A., HEMLEBEN, C., MEISCHNER, D. & ERLENKEUSER, H. (1996) Response of Red Sea Deep-Water Agglutinated Foraminifera to Water-Mass Changes During the Late Quaternary. *Mar. Micropal.*, **28,** 283-297.

AUGUSTIN, N., DEVEY, C.W., VAN DER ZWAN, F.M., FELDENS, P., TOMINAGA, M., BANTAN, R. & KWASNITSCHKA, T. (2014) The Transition from Rifting to Spreading in the Red Sea. *Earth Planet. Sci. Lett.*, **395,** 217-230.

BACHE, F., OLIVET, J.L., GORINI, C., RABINEAU, M., BAZTAN, J., ASLANIAN, D. & SUC, J.-P. (2009) Messinian Erosional and Salinity Crises: View from the Provence Basin (Gulf of Lions, Western Mediterranean). *Earth Planet. Sci. Lett.*, **286,** 139-157.

BADAWI, A., SCHMIEDL, G. & HEMLEBEN, C. (2005) Impact of Late Quaternary Environmental Changes on Deep-Sea Benthic Foraminiferal Faunas of the Red Sea. *Mar. Micropal.*, **58,** 13-30.

BECKER, J.J., SANDWELL, D.T., SMITH, W.H.F., BRAUD, J., BINDER, B., DEPNER, J., FABRE, D., FACTOR, J., INGALLS, S., KIM, S.-H., LADNER, R., MARKS, K., NELSON, S., PHARAOH, A., TRIMMER, R., VON ROSENBERG, J., WALLACE, G. & WEATHERALL, P. (2009) Global Bathymetry and Elevation Data at 30 Arc Seconds Resolution: SRTM30_Plus. *Marine Geodesy*, **32,** 355-371.

BERTONI, C. & CARTWRIGHT, J. (2005) 3D Seismic Analysis of Slope-Confined Canyons from the Plio-Pleistocene of the Ebro Continental Margin (Western Mediterranean). *Basin Res.*, **17,** 43-62.

BONATTI, E., BALL, M. & SCHUBERT, C. (1970) Evaporites and Continental Drift. *Naturwissenschaften*, **57,** 107-108.

BONATTI, E., COLANTONI, P., DELLA VEDOVA, B. & TAVIANI, M. (1984) Geology of the Red Sea Transitional Zone (22°N-25°N). *Oceanologica Acta*, **7,** 385-398.

BONATTI, E. (1985) Punctiform Initiation of Seafloor Spreading in the Red Sea During Transition from a Continental to an Oceanic Rift. *Nature*, **316,** 33-37.

BONATTI, E. & 24 OTHERS (2005) Geophysical, Geological and Oceanographic Surveys in the Northern Red Sea. Report on the Morphobathymetric, Magnetometric, Oceanographic, Coring and Dredging Investigations During Cruise Rs05 Aboard R/V Urania. Ismar Bologna Technical Report 94, Bologna March 2005, ISMAR. Bologna.

BOSWORTH, W., HUCHON, P. & MCCLAY, K. (2005) The Red Sea and Gulf of Aden Basins. *J. African Earth Sci.*, **43,** 334-378.

BOUDREAUX, J.E. (1974) Calcareous Nannoplankton Ranges, Deep Sea Drilling Project Leg 23. *in Whitmarsh, R.B., D. E. Wesser, D. A. Ross et al. Initial*

reports of the Deep Sea Drilling Project, U.S. Printing Office, **23,** 1073-1090.

BOUILLOUX, A., VALET, J.-P., BASSINOT, F., JORON, J.-L., DEWILDE, F., BLANC-VALLERON, M.-M. & MORENO, E. (2013) Influence of Seawater Exchanges across the Bab-El-Mandeb Strait on Sedimentation in the Southern Red Sea During the Last 60 Ka. *Paleocean.*, **28,** 675–687, doi:610.1002/2013PA002544.

BUNTER, M.A.G. & ABDEL MAGID, A.E.M. (1989) The Sudanese Red Sea: 1. New Developments in Stratigraphy and Petroleum-Geological Evolution. *J. Petrol. Geol.*, **12,** 145-166.

CANNAT, M., BRIAIS, A., DEPLUS, C., ESCARTíN, J., GEORGEN, J., LIN, J., MERCOURIEV, S., MEYZEN, C., MULLER, M., POULIQUEN, G., RABAIN, A. & DA SILVA, P. (1999) Mid-Atlantic Ridge–Azores Hotspot Interactions: Along-Axis Migration of a Hotspot-Derived Event of Enhanced Magmatism 10 to 4 Ma Ago. *Earth Panet. Sci. Lett.*, **173,** 257-269.

CHANG, S.-J. & VAN DER LEE, S. (2011) Mantle Plumes and Associated Flow beneath Arabia and East Africa. *Earth Planet Sci. Lett.*, **302,** 448-454.

CHU, D. & GORDON, R.G. (1998) Current Plate Motions across the Red Sea. *Geophys. J. Int.*, **135,** 313-328.

COCHRAN, J., R. (1979) An Analysis of Isostasy in the Worlds Oceans 2. Mid-Ocean Ridge Crests. *J. Geophys. Res.*, **84,** 4713-4729.

COCHRAN, J.R. (1983) A Model for the Development of the Red Sea. *Am. Assoc. Petrol. Geol. Bull.*, **67,** 41-69.

COCHRAN, J.R. (2005) Northern Red Sea: Nucleation of an Oceanic Spreading Center within a Continental Rift. *Geochemistry, Geophysics, Geosystems*, **6,** Paper Q03006, doi:03010.01029/02004GC000826.

COCHRAN, J.R. & KARNER, G.D. (2007) Constraints on the Deformation and Rupturing of Continental Lithosphere of the Red Sea: The Transition from Rifting to Drifting. In: *Imaging, Mapping and Modelling Continental Lithosphere Extension and Breakup, Spec. Publ. 282* (Ed. by G. D. Karner, G. Manatschal & L. M. Pinheiro), 265 - 289. Geological Society, London.

CORNÉE, J.-J., MÜNCH, P., MELINITE-DOBRINESCU, M., BEN MOUSSA, A., QUILLÉVÉRÉ, F., DRINIA, H., ZDIMOUSA, A., OUAZANI TOUHAMI, A., MERZERAUD, G., FAUQUETTE, S., CORSINI, M., MOISSETTE, P. & FEDDI, N. (2014) The Early Pliocene Reflooding in the Western Mediterranean: New Insights from the Rias of the Internal Rif, Morocco. *Comptes Rendus Geosc.*, **346,** 90-98.

CROSSLEY, R., WATKINS, C., RAVEN, M., CRIPPS, D., CARNELL, A. & WILLIAMS, D. (1992) The Sedimentary Evolution of the Red Sea and Gulf of Aden. *J. Petrol. Geol.*, **15,** 157-172.

DRAKE, C.L. & GIRDLER, R.W. (1964) A Geophysical Study of the Red Sea. *Geophys. J. Roy. Astr. Soc.*, **8,** 473-495.

EGLOFF, F., RIHM, R., MAKRIS, J., IZZELDIN, Y.A., BOBSIEN, M., MEIER, K., JUNGE, P., NOMAN, T. & WARSI, W. (1991) Contrasting Structural Styles of the Eastern and Western Margins of the Southern Red Sea: The 1988 Sonne Experiment. *Tectonophys.*, **198,** 329-353.

EHRHARDT, A., HÜBSCHER, C. & GAJEWSKI, D. (2005) Conrad Deep, Northern Red Sea: Development of an Early Stage Ocean Deep within the Axial Depression. *Tectonophys.*, **411,** 19-40.

EHRHARDT, A. & HÜBSCHER, C. (2015) The Northern Red Sea in Transition from Rifting to Drifting - Lessons Learned from Ocean Deeps. In: *The Red Sea:*

The Formation, Morphology, Oceanography and Environment of a Young Ocean Basin (Ed. by N. Rasul & I. C. Stewart), 99-121. Springer.

ELDERFIELD, H., FERRETTI, P., GREAVES, M., CROWHURST, S., MCCAVE, I.N., HODELL, D. & PIOTROWSKI, A.M. (2012) Evolution of Ocean Temperature and Ice Volume through the Mid-Pleistocene Climate Transition. *Science*, **337,** 704-709.

EVANS, R. (1978) Origin and Significance of Evaporites in Basins around Atlantic Margin. *Am Assoc. Petrol. Geol. Bull.*, **62,** 223-234.

FELDENS, P. & MITCHELL, N.C. (2015) Salt Flows in the Central Red Sea. In: *The Red Sea: The Formation, Morphology, Oceanography and Environment of a Young Ocean Basin* (Ed. by N. Rasul & I. C. Stewart), 205-218. Springer.

FENTON, M., GEISELHART, S., ROHLING, E.J. & HEMLEBEN, C. (2000) Aplanktonic Zones in the Red Sea. *Mar. Micropal.*, **40,** 277-294.

FOURNIER, M., CHAMOT-ROOKE, N., PETIT, C., HUCHON, P., AL-KATHIRI, A., AUDIN, L., BESLIER, M.-O., D'ACREMONT, E., FABBRI, O., FLEURY, J.M., KHANBARI, K., LEPVRIER, C., LEROY, S., MAILLOT, B. & MERKOURIEV, S. (2010) Arabia-Somalia Plate Kinematics, Evolution of the Aden-Owen-Carlsberg Triple Junction, and Opening of the Gulf of Aden. *J. Geophys. Res.*, **116,** doi:10.1029/2008JB006257.

GARFUNKEL, Z., GINZBURG, A. & SEARLE, R.C. (1987) Fault Pattern and Mechanism of Crustal Separation Along the Axis of the Red Sea from Side Scan Sonar (GLORIA) Data. *Annales Geophysicae*, **5B,** 187-200.

GAULIER, J.M., LEPICHON, X., LYBERIS, N., AVEDIK, F., GELY, L., MORETTI, I., DESCHAMPS, A. & HAFEZ, S. (1988) Seismic Study of the Crustal Thickness, Northern Red Sea and Gulf of Suez. *Tectonophysics*, **153,** 55-88.

GIRDLER, R.W. (1970) A Review of Red Sea Heat Flow. *Phil. Trans. Roy. Soc. ser. A*, **267,** 191-203.

GIRDLER, R.W. & STYLES, P. (1974) Two Stage Red Sea Floor Spreading. *Nature* **247,** 1-11.

GIRDLER, R.W. & WHITMARSH, R.B. (1974) Miocene Evaporites in Red Sea Cores, Their Relevance to the Problem of the Width and Age of Oceanic Crust beneath the Red Sea. In: *Initial Reports of the Deep Sea Drilling Project, Vol. 23* (Ed. by R. B. Whitmarsh, O. E. Weser, D. A. Ross et al.), 913-921. U.S. Govt. Printing Office, Washington, D.C.

GRADSTEIN, F.M. & OGG, J.G. (2004) Geological Time Scale 2004 - Why, How, and Where Next! *Lethaia*, **37,** 175-181.

GUENNOC, R., PAUTOT, G. & COUTELLE, A. (1988) Surficial Structures of the Northern Red Sea Axial Valley from 23°N to 28°N: Time and Spare Evolution of the Neooceanic Structures. *Tectonophysics*, **153,** 1-23.

GVIRTZMAN, Z., RESHEF, M., BUCH-LEVIATAN, O. & BEN-AVRAHAM, Z. (2013) Intense Salt Deformation in the Levant Basin in the Middle of the Messinian Salinity Crisis. *Earth Planet Sci. Lett.*, **379,** 108-119.

HAASE, K.M., MÜHE, R. & STOFFERS, P. (2000) Magmatism During Extension of the Lithosphere: Geochemical Constraints from Lavas of the Shaban Deep, Northern Red Sea. *Chem. Geol.*, **166,** 225-239.

HALL, S.A. (1989) Magnetic Evidence for the Nature of the Crust beneath the Southern Red Sea. *J. Geophs. Res.*, **94,** 12267-12279.

HEMLEBEN, C., ET AL. (1996) Three Hundred Eighty Thousand Year Long Stable Isotope and Faunal Records from the Red Sea: Influence of Global Sea Level Change on Hydrography. *Paleoceanography*, **11,** 147–156.

HOFMANN, P., SCHWARK, L., BRACHERT, T., BADAUT, D., RIVIÈRE, M. & PURSER, B.H. (1998) Sedimentation, Organic Geochemistry and Diagenesis of Cores from the Axial Zone of the Southern Red Sea: Relationships to Rift Dynamics and Climate. In: *Sedimentation and Tectonics of Rift Basins: Red Sea-Gulf of Aden* (Ed. by B. H. Purser & D. W. J. Bosence), 479-504. Chapman & Hall, London.

HÜBSCHER, C. & NETZEBAND, G.L. (2007) Evolution of a Young Salt Giant: The Example of the Messinian Evaporites in the Levantine Basin. In: *The Mechanical Behaviour of Salt – Understanding of THMC Processes in Salt* (Ed. by M. Wallner, K.-H. Lux, W. Minkley & J. Hardy, H.R.), 175-184. Taylor & Francis Group, London.

HÜBSCHER, C., TAHCHI, E., KLAUCKE, I., MAILLARD, A. & SAHLING, H. (2009) Salt Tectonics and Mud Volcanism in the Latakia and Cyprus Basins, Eastern Mediterranean. *Tectonophys.*, **470,** 173-182.

HUDEC, M.R. & JACKSON, M.P.A. (2006) Advance of Allochthonous Salt Sheets in Passive Margins and Orogens. *Am Assoc. Petrol. Geol. Bull.*, **90,** 1535-1564.

HUGHES, G.W. & BEYDOUN, Z.R. (1992) The Red Sea - Gulf of Aden: Biostratigraphy, Lithostratigraphy and Palaeoenvironments. *J. Petrol. Geol.*, **15,** 135-156.

HUGHES, G.W. (2014) Micropalaeontology and Palaeoenvironments of the Miocene Wadi Waqb Carbonate of the Northern Saudi Arabian Red Sea. *GeoArabia*, **19,** 59-108.

HUTCHINSON, R.W. & ENGELS, G.G. (1972) Tectonic Evolution in the Southern Red Sea and Its Possible Significance to Older Rifted Continental Margins. *Geol. Soc. Am. Bull.*, **83,** 2989-3002.

ITO, G. (2001) Reykjanes 'V'-Shaped Ridges Originating from a Pulsing and Dehydrating Mantle Plume. *Nature*, **411,** 681-684.

IZZELDIN, A.Y. (1982) On the Structure and Evolution of the Red Sea. *PhD Thesis, Universite Louis Pasteur***,** 163p.

IZZELDIN, A.Y. (1987) Seismic, Gravity and Magnetic Surveys in the Central Part of the Red Sea: Their Interpretation and Implications for the Structure and Evolution of the Red Sea. *Tectonophysics*, **143,** 269-306.

IZZELDIN, A.Y. (1989) Transverse Structures in the Central Part of the Red Sea and Implications on Early Stages of Oceanic Accretion. *Geophys. J.*, **96,** 117-129.

KNOTT, S.T., BUNCE, E.T. & CHASE, R.L. (1966) Red Sea Seismic Reflection Studies *in The World Rift System, Geol. Surv. Canada, Paper 66-14,* 78-97.

LABRECQUE, J.L. & ZITELLINI, N. (1985) Continuous Seafloor Spreading in the Red Sea: An Alternative Interpretation of the Magnetic Anomaly Pattern. *A.A.P.G. Bull.*, **69,** 513-524.

LIGI, M., BONATTI, E., TONTINI, F.C., CIPRIANI, A., COCCHI, L., SCHETTINO, A., BORTOLUZZI, G., FERRANTE, V., KHALIL, S., MITCHELL, N.C. & RASUL, N. (2011) Initial Burst of Oceanic Crust Accretion in the Red Sea Due to Edge-Driven Mantle Convection. *Geology*, **39,** 1019-1022.

LIGI, M., BONATTI, E., BORTOLUZZI, G., CIPRIANI, A., COCCHI, L., CARATORI TONTINI, F., CARMINATI, E., OTTOLINI, L. & SCHETTINO, A. (2012) Birth of an Ocean in the Red Sea: Initial Pangs. *Geochem. Geophys. Geosys.*, **13,** Paper Q08009, doi:08010.01029/02012GC004155.

LOCKE, S. & THUNELL, R.C. (1988) Paleoceanographic Record of the Last Glacial/Interglacial Cycle in the Red Sea and Gulf of Aden. *Palaeogeog.,*

Palaeoclim. Palaeoecol., **64,** 163-187.

LOUDEN, K.E. & FORSYTH, D.W. (1982) Crustal Structure and Isostatic Compensation near the Kane Fracture Zone from Topography and Gravity Measurements - I. Spectral Analysis Approach. *Geophys. J. Roy. astr. Soc.*, **68,** 725-750.

MACKENZIE, K.V. (1981) Discussion of Sea-Water Sound-Speed Determinations. *J. Acoust. Soc. Am.*, **70,** 801-806.

MAKRIS, J., HENKE, C.H., EGLOFF, F. & AKAMALUK, T. (1991) The Gravity Field of the Red Sea and East Africa. *Tectonophys.*, **198,** 369-381.

MANHEIM, F.T., DWIGHT, L. & BELASTOCK, R.A. (1974) Porosity, Density, Grain Density, and Related Physical Properties of Sediments from the Red Sea Drill Cores. In: *Initial Reports of the Deep Sea Drilling Project, Vol. 23* (Ed. by R. B. Whitmarsh, O. E. Weser, D. A. Ross et al.), 887-907. U.S. Govt. Printing Office, Washington, D.C.

MARTY, J.C. & CAZENAVE, A. (1989) Regional Variations in Subsidence Rate of Oceanic Plates: A Global Analysis. *Earth Planet. Sci. Lett.*, **94,** 301-315.

MCKENZIE, D. (1978) Some Remarks on the Development of Sedimentary Basins. *Earth Planet. Sci. Lett.*, **40,** 25-32.

MILKEREIT, B. & FLUH, E.R. (1985) Saudi Arabian Refraction Profile: Crustal Structure of the Red Sea-Arabian Shield Transition. *Tectonophysics*, **111,** 283-298.

MILLER, P.M. & BARAKAT, H. (1988) Geology of the Safaga Concession, Northern Red Sea, Egypt. *Tectonophysics*, **153,** 123-136.

MITCHELL, D.J.W., ALLEN, R.B., SALAMA, W. & ABOUZAKM, A. (1992) Tectonostratigraphic Framework and Hydrocarbon Potential of the Red Sea. *J. Petrol. Geol.*, **15,** 187-210.

MITCHELL, N.C., LIGI, M., FARRANTE, V., BONATTI, E. & RUTTER, E. (2010a) Submarine Salt Flows in the Central Red Sea. *Geol. Soc. Am. Bull.*, **122,** 701-713.

MITCHELL, N.C., SCHMIDT, M. & LIGI, M. (2010b) Comment on "Formation of Thetis Deep Metal-Rich Sediments in the Absence of Brines, Red Sea" by Pierret et al. (2010). *J. Geochem. Expl.*, **108,** 112-113.

MITCHELL, N.C. & PARK, Y. (2014) Nature of Crust in the Central Red Sea. *Tectonophys.*, **628,** 123-139.

MITCHELL, N.C. (2015) Lineaments in Gravity Data of the Red Sea. In: *The Red Sea: The Formation, Morphology, Oceanography and Environment of a Young Ocean Basin* (Ed. by N. Rasul & I. C. Stewart), 123-133. Springer.

MOONEY, W.D., GETTINGS, M.E., BLANK, H.R. & HEALY, J.H. (1985) Saudi Arabian Seismic-Refraction Profile: A Traveltime Interpretation of Crustal and Upper Mantle Structure. *Tectonophys.*, **111,** 173-246.

NETZEBAND, G.L., HüBSCHER, C. & GAJEWSKI, D. (2006) The Structural Evolution of the Messinian Evaporites in the Levantine Basin. *Mar. Geol.*, **230,** 249-273.

ORSZAG-SPERBER, F., HARWOOD, G., KENDALL, A. & PURSER, B.H. (1998) Review of the Evaporites of the Red Sea-Gulf of Suez Rift. In: *Sedimentation and Tectonics of Rift Basins: Red Sea-Gulf of Aden* (Ed. by B. H. Purser & D. W. J. Bosence), 409-426. Chapman & Hall, London.

PALCHAN, D., STEIN, M., ALMOGI-LABIN, A., EREL, Y. & GOLDSTEIN, S.L. (2013) Dust Transport and Synoptic Conditions over the Sahara–Arabia Deserts During the MIS6/5 and 2/1 Transitions from Grain-Size, Chemical and Isotopic Properties of Red Sea Cores. *Earth Planet. Sci. Letts.*, **382,** 125-

139.

PAUTOT, G., AUZENDE, J.M. & LEPICHON, X. (1966) Continuous Deep Salt Layer Along North Atlantic Margins Related to Early Phase of Rifting. *Nature*, **227,** 351-354.

PAUTOT, G. (1983) Les Fosses De La Mer Rouge: Approche Geomorphologique d'un Stade Initial D'ouvertur Oceanique Realisee a L'aide du Seabeam. *Oceanologica Acta*, **6,** 235-244.

PETZOLD, M. (1986) Untersuchungen Zur Horizontal- Und Vertikalverteilung Des Phytoplanktons Im Roten Meer, Univ. Hamburg, Hamburg, Germany.

PFANNKUCHE, O. (1993) Benthic Standing Stock and Metabolic Activity in the Bathyal Red Sea from 17°N to 27°N. *Mar. Ecol.*, **14,** 67-79.

PHILLIPS, J.D. & ROSS, D.A. (1970) Continuous Seismic Reflexion Profiles in the Red Sea. *Phil. Trans. Roy. Soc. London*, **267 series A,** 143-152.

REICHE, S., HüBSCHER, C. & BEITZ, M. (2014) Fault-Controlled Evaporite Deformation in the Levant Basin, Eastern Mediterranean. *Mar. Geol.*, **354,** 53-68.

ROBERTS, A.P., ROHLING, E.J., GRANT, K.M., LARRASOAÑA, J.C. & LIU, Q. (2011) Atmospheric Dust Variability from Arabia and China over the Last 500,000 Years. *Quat. Sci. Rev.*, **30,** 3537-3541.

ROESER, H.A. (1975) A Detailed Magnetic Survey of the Southern Red Sea. *Geol. Jahrb. 13***,** 131-153.

RONA, P.A. (1982) Evaporites at Passive Margins. In: *Dynamics of Passive Margins* (Ed. by R. A. Scrutton), **Geodyn. Ser. Vol. 6**, 116-132. Am. Geophys. Union and Geol. Soc. Am.

ROONEY, T.O., HARZBERG, C. & BASTOW, I.D. (2012) Elevated Mantle

Temperature beneath East Africa. *Geology*, **40,** 27-30.

ROSS, D.A. & SCHLEE, J. (1973) Shallow Structure and Geologic Development of the Southern Red Sea. *Geol. Soc. Am. Bull.*, **84,** 3827-3848.

SANDWELL, D., MÜLLER, R.D., SMITH, W.H.F., GARCIA, E. & FRANCIS, R. (2014) New Global Marine Gravity Model from Cryosat-2 and Jason-1 Reveals Buried Tectonic Structure. *Science*, **346,** 65-67.

SANDWELL, D.T. & SMITH, W.H.F. (1997) Marine Gravity Anomaly from Geosat and Ers-1 Satellite Altimetry. *J. Geophys. Res.*, **102,** 10039-10054.

SCHMIDT, M., DEVEY, C., EISENHAUER, A. & CRUISE PARTICIPANTS (2011) FS Poseidon Cruise Report P408, Christian-Albrechts University of Kiel. Kiel**,** 80.

SCHMIDT, M., AL-FARAWATI, R., AL-AIDAROOS, A. & KÜRTEN, B.E. (2013) RV Pelagia Fahrtbericht / Cruise Report 64pe350/64pe351 – Jeddah-Transect ; 08.03. – 05.04.2012 Jeddah - Jeddah, 06.04 - 22.04.2012 Jeddah - Duba, Geomar Report, N. Ser. 005, GEOMAR Helmholtz-Zentrum für Ozeanforschung, Kiel. Kiel, Germany**,** 154 pp., DOI:110.3289/GEOMAR_REP_NS_3285_2013.

SEARLE, R.C. & ROSS, D.A. (1975) A Geophysical Study of the Red Sea Axial Trough between 20.5° and 22°N. *Geophys. J. Roy. Astr. Soc.*, **43,** 555-572.

SMITH, W.H.F. & WESSEL, P. (1990) Gridding with Continuous Curvature Splines in Tension. *Geophysics*, **55,** 293-305.

SOFIANOS, S.S. & JOHNS, E.W. (2007) Observations of the Summer Red Sea Circulation. *J. Geophys. Res.*, **112,** Paper C06025, doi:06010.01029/02006JC003886.

SPIERS, C.J., SCHUTJENS, P.M.T.M., BRZESOWSKY, R.H., PEACH, C.J., LIEZENBERG,

J.L. & ZWART, H.J. (1990) Experimental Determination of Constitutive Parameters Governing Creep of Rocksalt by Pressure Solution. In: *Deformation Mechanisms, Rheology and Tectonics, Geol. Soc. Spec. Publ. 54* (Ed. by R. J. Knipe & E. H. Rutter), 215-227. Geol. Soc., London.

STEIN, M., ALMOGI-LABIN, A., GOLDSTEIN, S.L., HEMLEBEN, C. & STARINSKY, A. (2007) Late Quaternary Changes in Desert Dust Inputs to the Red Sea and Gulf of Aden from $^{87}Sr/^{86}Sr$ Ratios in Deep-Sea Cores. *Earth Planet Sci. Lett.*, **261,** 104-119.

STOFFERS, P. & KüHN, R. (1974) Red Sea Evaporites: A Petrographic and Geochemical Study. In: *Initial Reports of the Deep Sea Drilling Project, Vol. 23* (Ed. by R. B. Whitmarsh, O. E. Weser, D. A. Ross et al.), 821-847. U.S. Govt. Printing Office, Washington, D.C.

STOFFERS, P. & ROSS, D.A. (1974) Sedimentary History of the Red Sea. *in: Whitmarsh, R.B., O.E. Weser, D.A. Ross, et al., Initial reports of the Deep Sea Drilling Project U.S. Government Printing Office*, **23,** 849-865.

TIBERI, C., EBINGER, C., BALLU, V., STUART, G. & OLUMA, B. (2005) Inverse Models of Gravity Data from the Red Sea-Aden-East African Rifts Triple Junction Zone. *Geophys. J. Int.*, **163,** 775-787.

TRAMONTINI, C. & DAVIES, D. (1969) A Seismic Refraction Survey in the Red Sea. *Geophys. J. R. Astr. Soc.*, **17,** 225-241.

TURCOTTE, D.L. & SCHUBERT, G. (1982) *Geodynamics: Applications of Continuum Physics to Geological Problems*. John Wiley and Sons, New York.

VOGT, P.R. (1979) Global Magmatic Episodes: New Evidence and Implications for the Steady-State Mid-Ocean Ridge. *Geology*, **7,** 93-98.

WESSEL, P. & SMITH, W.H.F. (1991) Free Software Helps Map and Display Data.

Eos, Transactions, American Geophysical Union, **72,** 441.

WHEILDON, J., EVANS, T.R. & GIRDLER, R.W. (1974) Thermal Conductivity, Density, and Sonic Velocity Measurements of Samples of Anhydrite and Halite from Sites 225 and 227. In: *Initial Reports of the Deep Sea Drilling Project, Vol. 23* (Ed. by R. B. Whitmarsh, O. E. Weser, D. A. Ross et al.), 909-911. U.S. Govt. Printing Office, Washington, D.C.

WHITMARSH, R.B. (1974) Appendix V: Geophysical Appendix. *in Whitmarsh, R.B., D. E. Wesser, D. A. Ross et al. Initial reports of the Deep Sea Drilling Project, U.S. Printing Office*, **23,** 1159-1171.

WHITMARSH, R.B., WESER, O.E. & ROSS, D.A. (1974) *Initial Reports of the Deep Sea Drilling Project, 23b*. U. S. Government Printing Office, Washington, D. C.

WILSON, J.W.P., ROBERTS, G.G., HOGGARD, M.J. & WHITE, N.J. (2014) Cenozoic Epeirogeny of the Arabian Peninsula from Drainage Modeling. *Geochem. Geophys. Geosys.*, **15,** 3723– 3761, doi:3710.1002/2014GC005283.

Figures

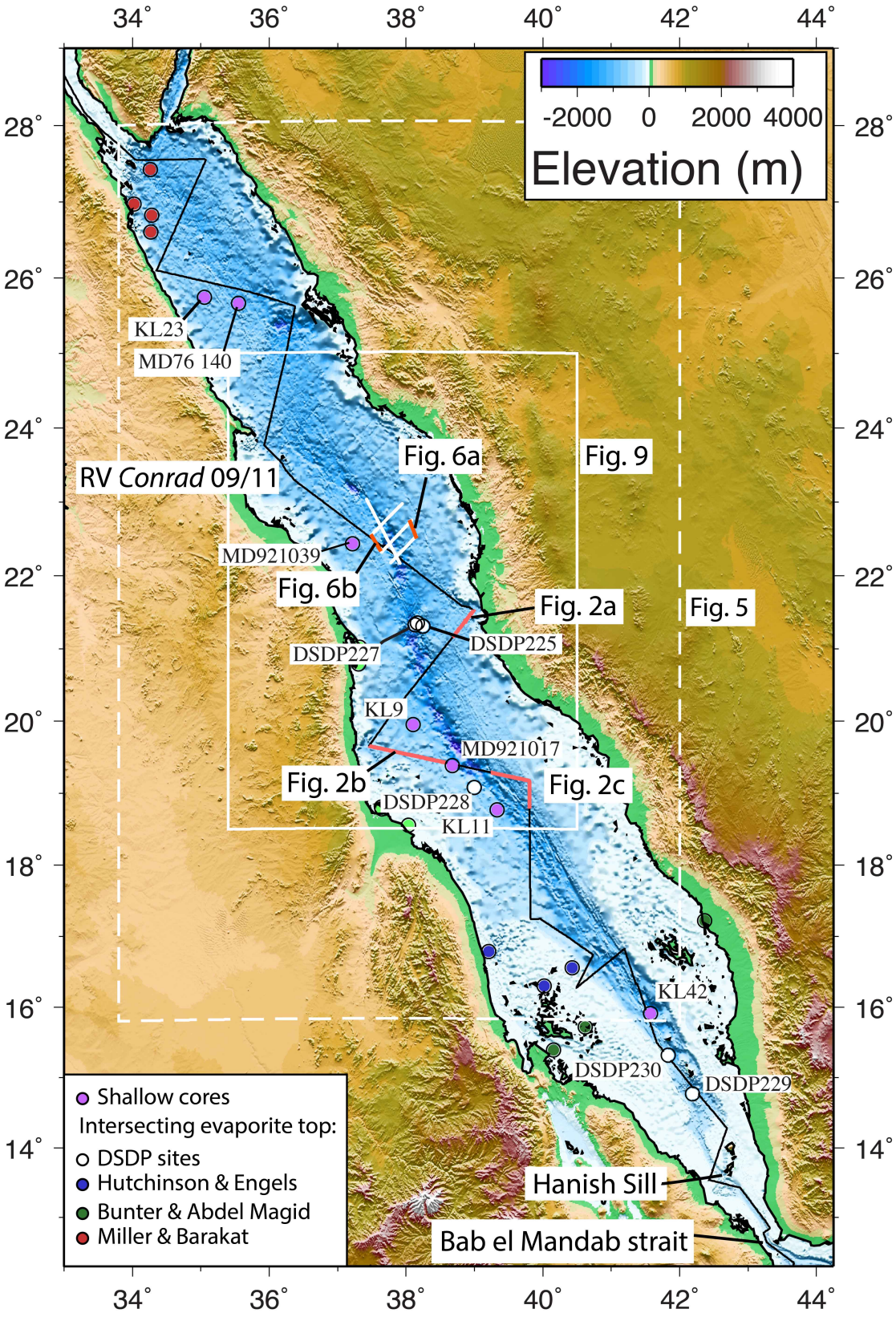

Figure 1. Overview of the Red Sea physiography along with paths of RVs *Conrad* (black, cruise RC0911) and *Urania* (white (Bonatti & and_24_others, 2005)). Red

lines locate examples of seismic reflection data in Figures 2 and 6. Purple-filled circles locate shallow sediment cores summarized in Figure 4. Boreholes intersecting the top of the evaporites or other salt deposits include (red-filled circles) Miller and Barakat (1988), (light green) Bunter and Abdel Magid (1989), (dark green) Girdler (1970) and (blue) Hutchinson and Engels (1972).

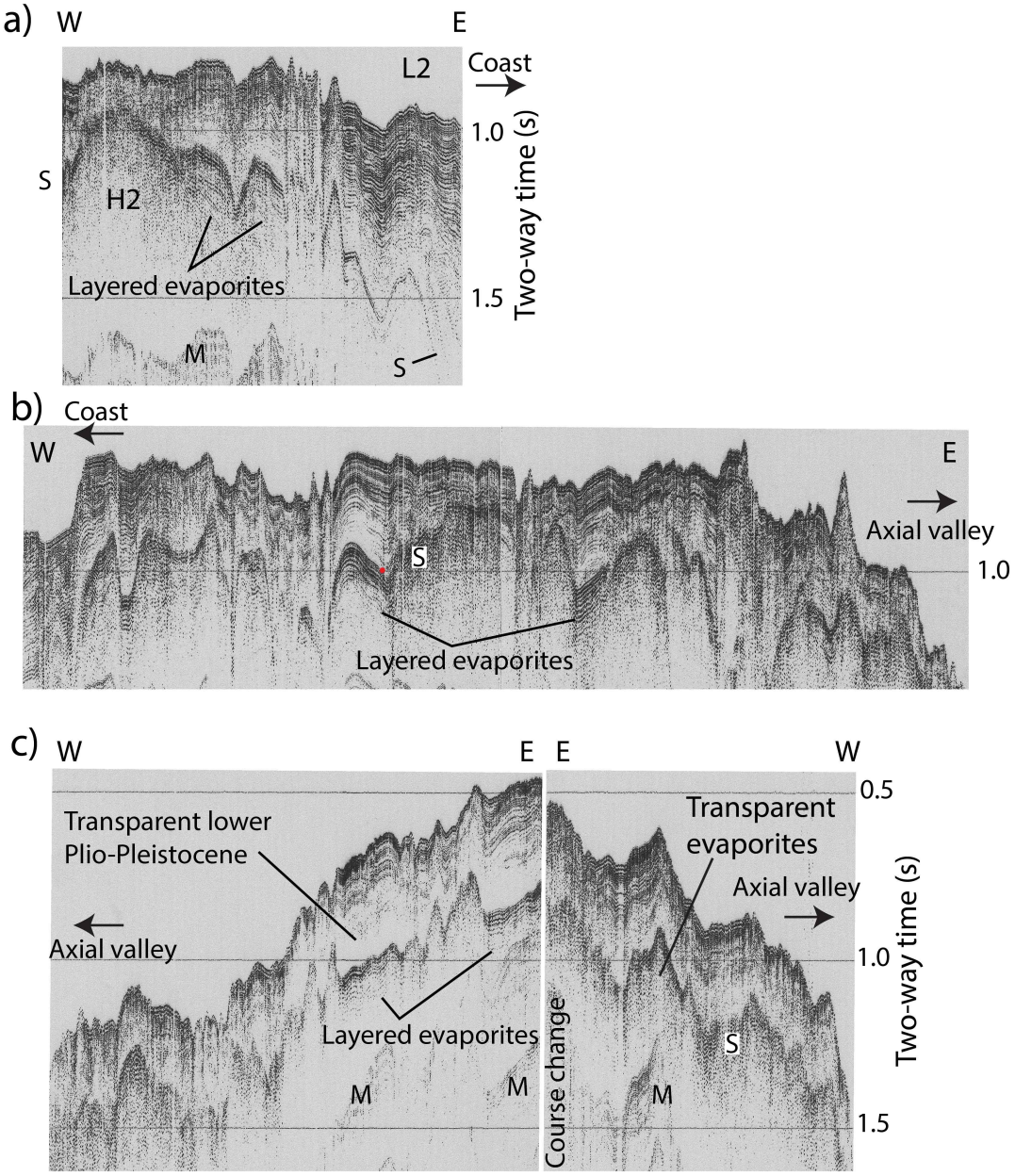

Figure 2. Selection of seismic reflection data acquired during RV *Conrad* cruise RC0911 located in Figure 1. S: reflection S. M: multiple reflection. Solid red

circle in (b) locates an elevation of S discussed in the text, where S appears not to be an unconformity at the scale of the seismic data. L2 and H2 in (a) correspond with annotation in Figure 9.

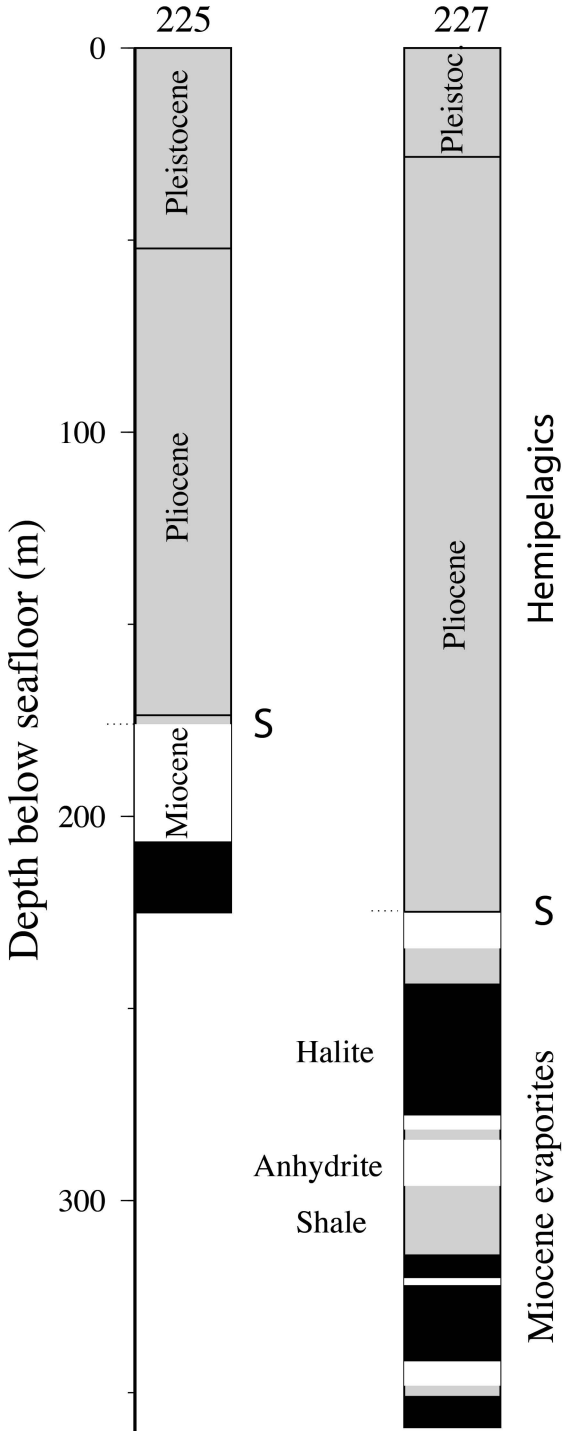

Figure 3. Stratigraphy at DSDP Sites 225 and 227 (Stoffers & Kühn, 1974; Whitmarsh *et al.*, 1974). Grey fill represents the Plio-Pleistocene hemipelagics above the S reflection and shale within the evaporites. White and black fill represent anhydrite and halite, respectively. "S" represents where the S reflection is expected in seismic data if at the top of the Miocene.

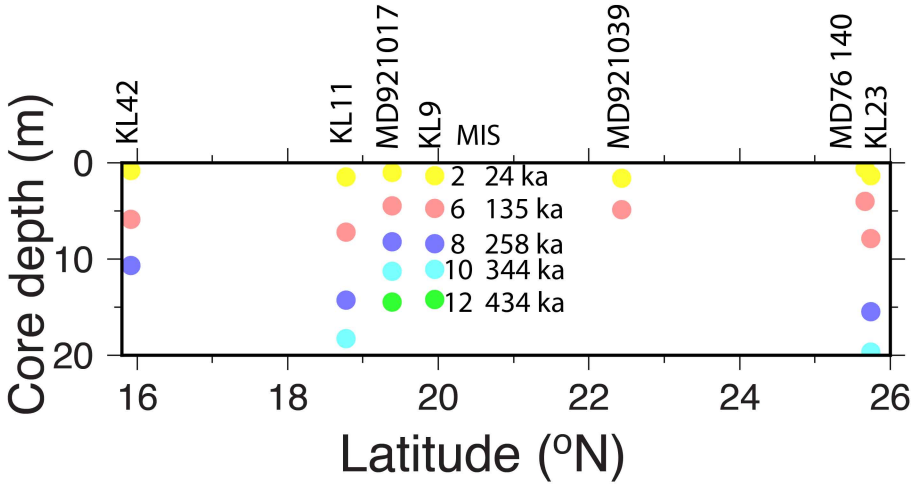

Figure 4. Depths of Marine Isotope Stages (MIS) within shallow sediment cores located in Figure 1 (colours correspond to the stages marked in the centre of the graph along with their ages (from Elderfield et al. (2012))). The sources of ^{18}O stratigraphy include (KL42) Badawi et al. (2005), (KL11) Hemleben et al. (1996), (MD921017) Fenton et al. (2000), (KL9), (MD921039) Fenton et al. (2000), (MD76140) Almogi-Labin et al. (1986) and (KL23) Badawi et al. (2005). Where samples were missing within glacial maxima but locations were clear, the stage was estimated by interpolation. Similarly, MIS 6 in MD76140 was obtained by modest extrapolation.

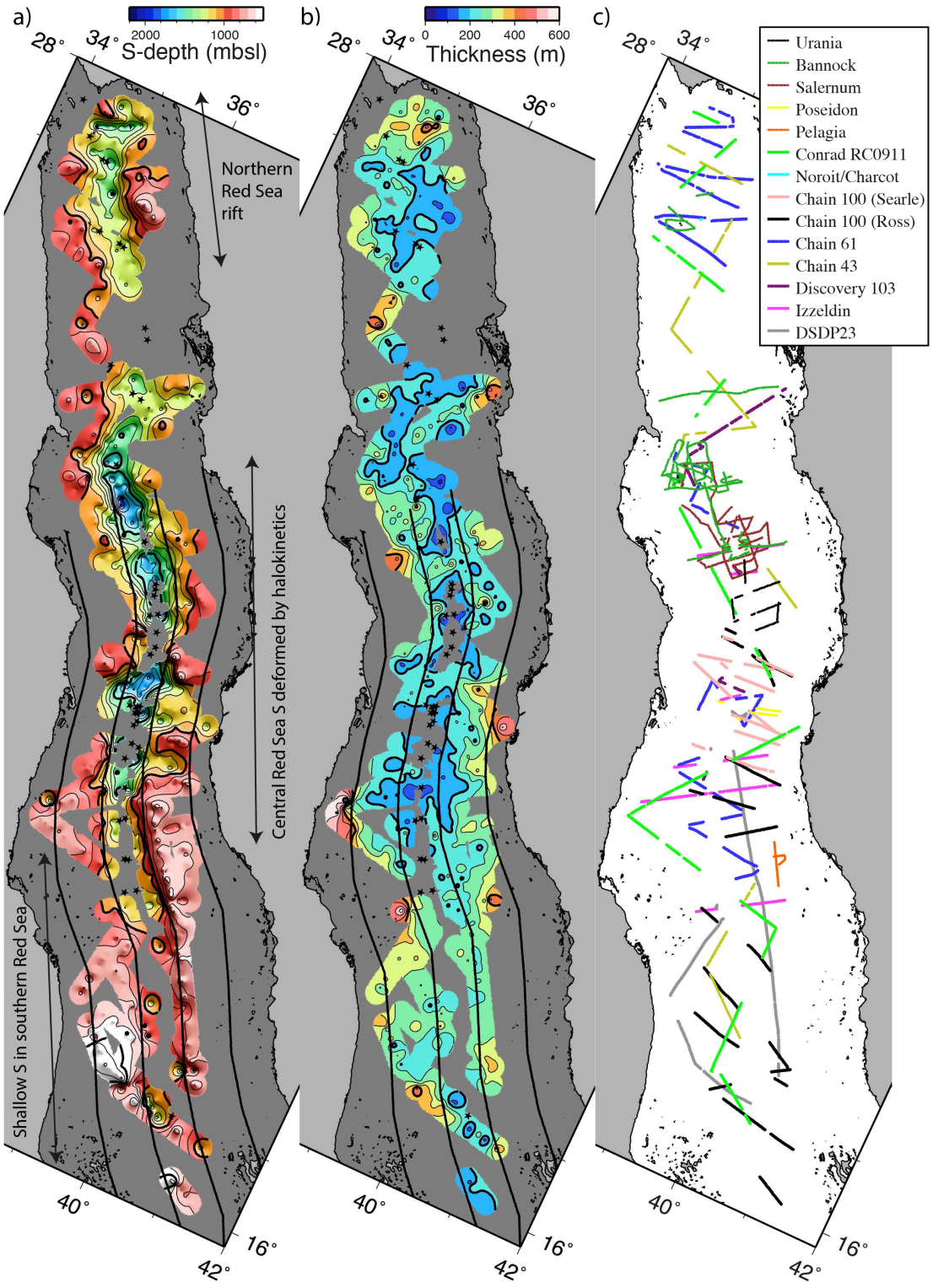

Figure 5. (a) Depth of the S-reflection below sea level (artificial lighting from due north). Pairs of lines either side of the rift axis in this and panel (b) are corridors over which data were selected to analyze regional trends (Figure 8). Solid star symbols in this and panel (b) are locations of deeps compiled by Augustin et al.

(2014). (b) Thickness of Plio-Pleistocene sediment overlying S. (c) Key to cruise data used (see main text for sources).

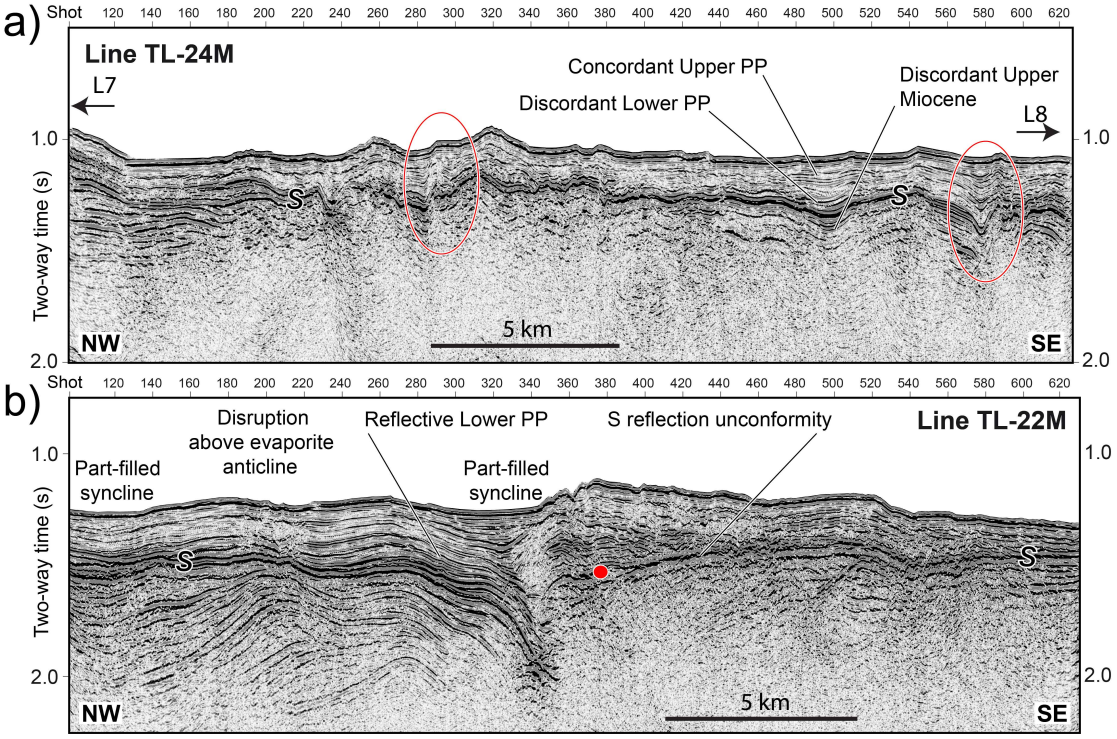

Figure 6. Selection of seismic reflection data acquired in 2005 on RV *Urania* located in Figure 1. (a) Line TL24M. (b) Line TL22M. Only a spherical divergence time-varying gain correction has been applied to amplitudes. The data have been filtered with a single band-pass filter (12-18 to 180-240 Hz) and migrated. S: reflection S. L7 and L8: lows from Figure 9. Ellipses in (a) highlight stratigraphy showing smaller gradients in upper Plio-Pleistocene strata than in the uppermost Miocene and/or S reflection (possible tectonic growth structures). Solid red circle in (b) locates an elevation of S discussed in the text, where S appears unconformably to truncate underlying evaporite reflections.

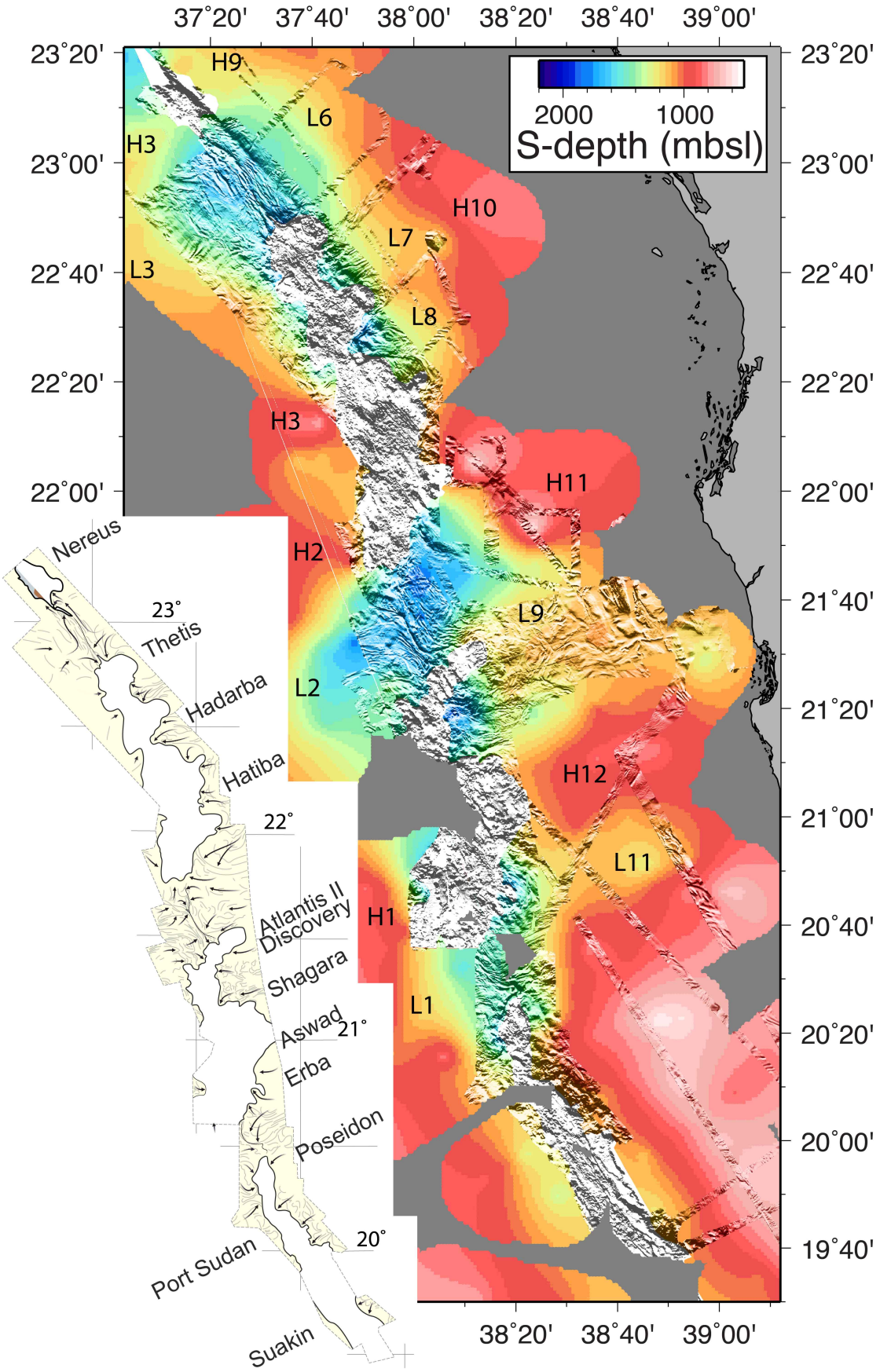
37°20'
37°40'
38°00'
38°20'
38°40'
39°00'
23°20'
23°00'
22°40'
22°20'
22°00'
21°40'
21°20'
21°00'
20°40'
20°20'
20°00'
19°40'
2000
1000
S-depth (mbsl)
H9
L6
H3
H10
L7
L3
L8
H3
H11
H2
L9
L2
H12
L11
H1
L1
Nereus
23°
Thetis
Hadarba
Hatiba
22°
Atlantis II
Discovery
Shagara
Aswad
21°
Erba
Poseidon
20°
Port Sudan
Suakin

Figure 7. Combined map of S-reflection depths (colours, mbsl) with shading from the multibeam sonar data (Pautot, 1983; Mitchell *et al.*, 2010a; Augustin *et al.*, 2014). Colour contour interval in this figure is 50 m, otherwise colours are as in Figures 5 and 9. Lower-left inset shows the interpreted extent of evaporite and other sedimentary cover of Augustin et al. (2014). Grey shading without colour in the centre of the main panel represents areas of volcanic geomorphology in the interpretation of Augustin et al. (2014). Lettering L1, H1, etc., as Figure 9.

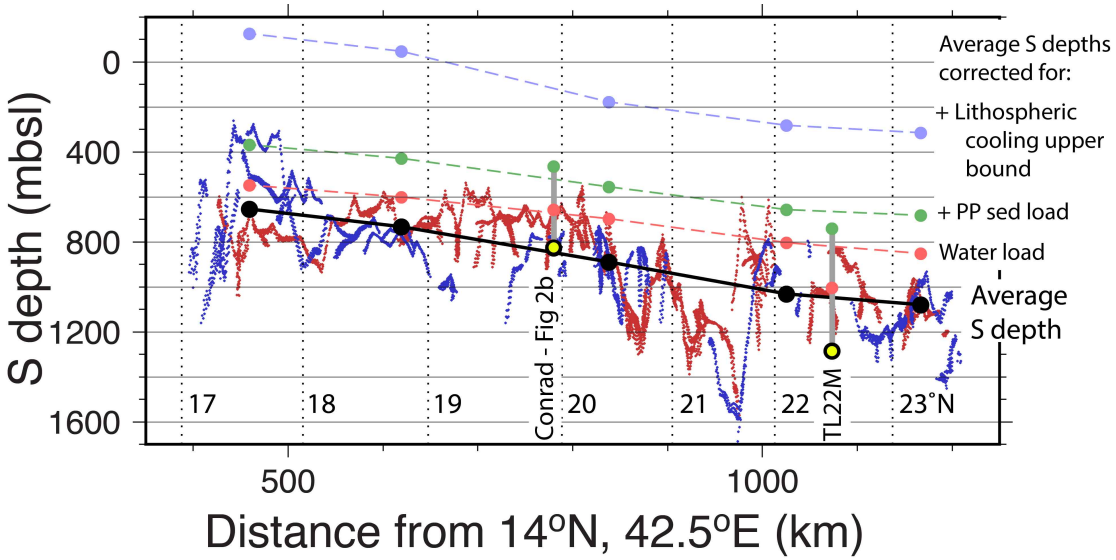

Figure 8. Along-rift variation of depth of the S reflection. Blue and red represent values from the west and east sides of the rift, respectively (Figure ES3). Black solid circles connected by solid lines are averages computed every 200 km. Three further lines show the S depth corrected successively for (pink) water load, (light green) PP sediment load and (light blue) an upper bound of lithospheric cooling (see main text for details). Vertical dotted lines represent latitudes of the rift axis. Similar calculations are shown (grey bars) for two sites where S (depths marked by open yellow circles) was apparently unaffected by

erosion (from Figure 2b) and where it forms a sharp unconformity (TL22M from Figure 6b).

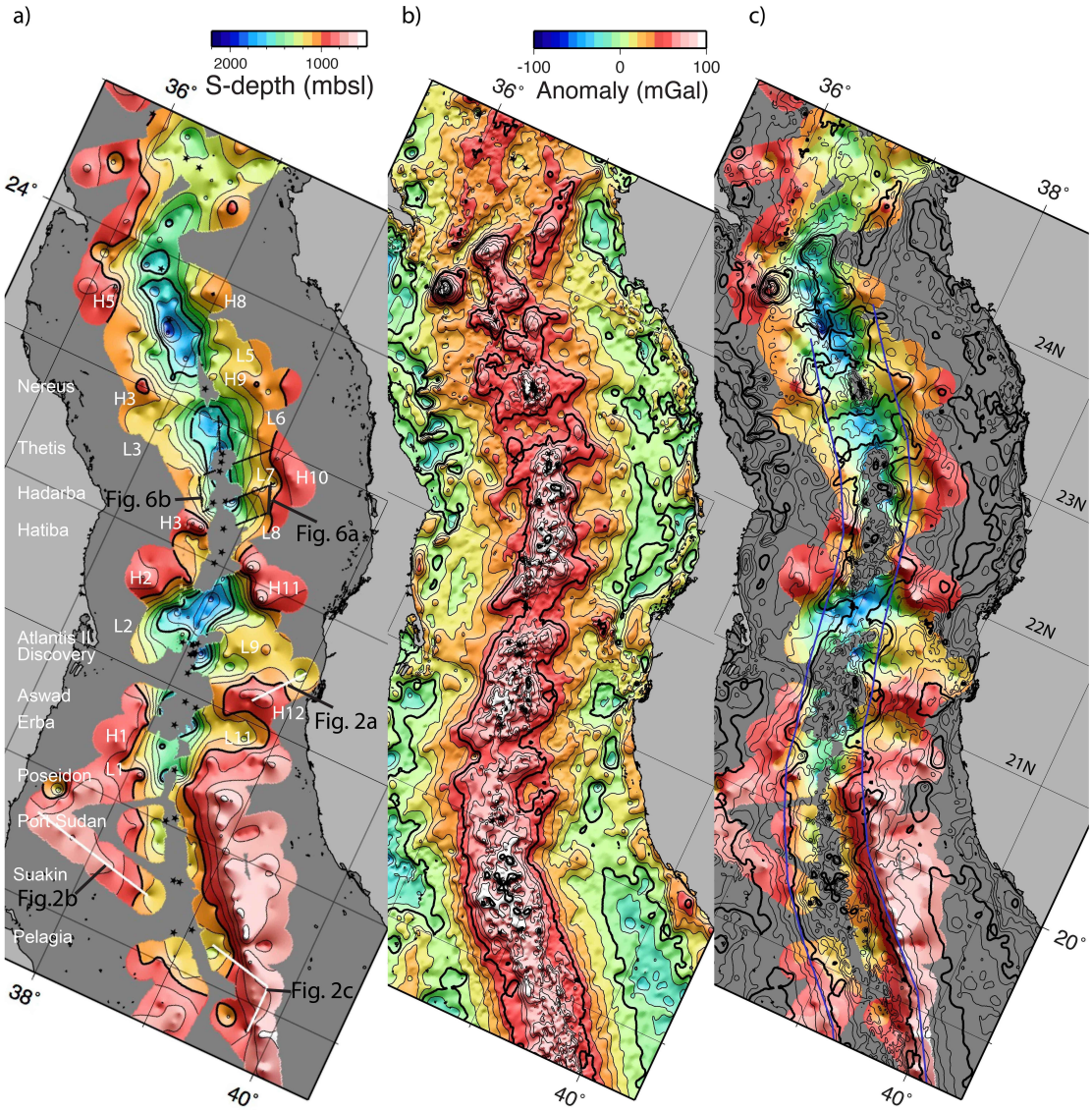

Figure 9. Enlargements covering the central Red Sea. (a) S-reflection depth (mbsl). Solid star symbols locate deeps compiled by Augustin et al. (2014) (a selection of names of deeps are given along left edge of panel). Annotation L1 to L11 and H1 to H12 are S-reflection lows and highs referred to in the text. (b) Version 22 of the marine free-air gravity field derived from satellite altimeter measurements by David Sandwell and co-workers (www.topex.ucsd.edu), which

is similar to their version 23 (Sandwell *et al.*, 2014). Anomalies have been corrected for seabed topography using a density contrast of 1.13 g cm^{-3} (i.e., marine Bouguer anomalies). (c) Combined plot with S depth (colour scale as Figure 9a) overlain with the 10-mGal contours from (b). Blue lines represent the total opening between Nubia and Arabia since 5.3 Ma predicted using the rotation pole of Chu and Gordon (1998).

Electronic supplement

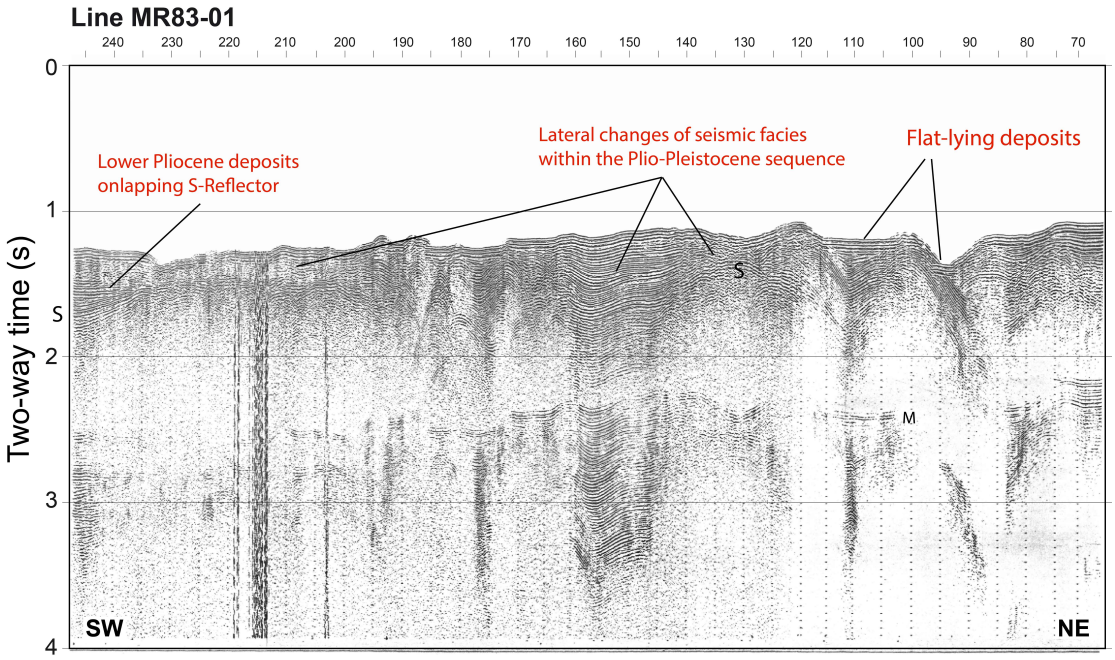

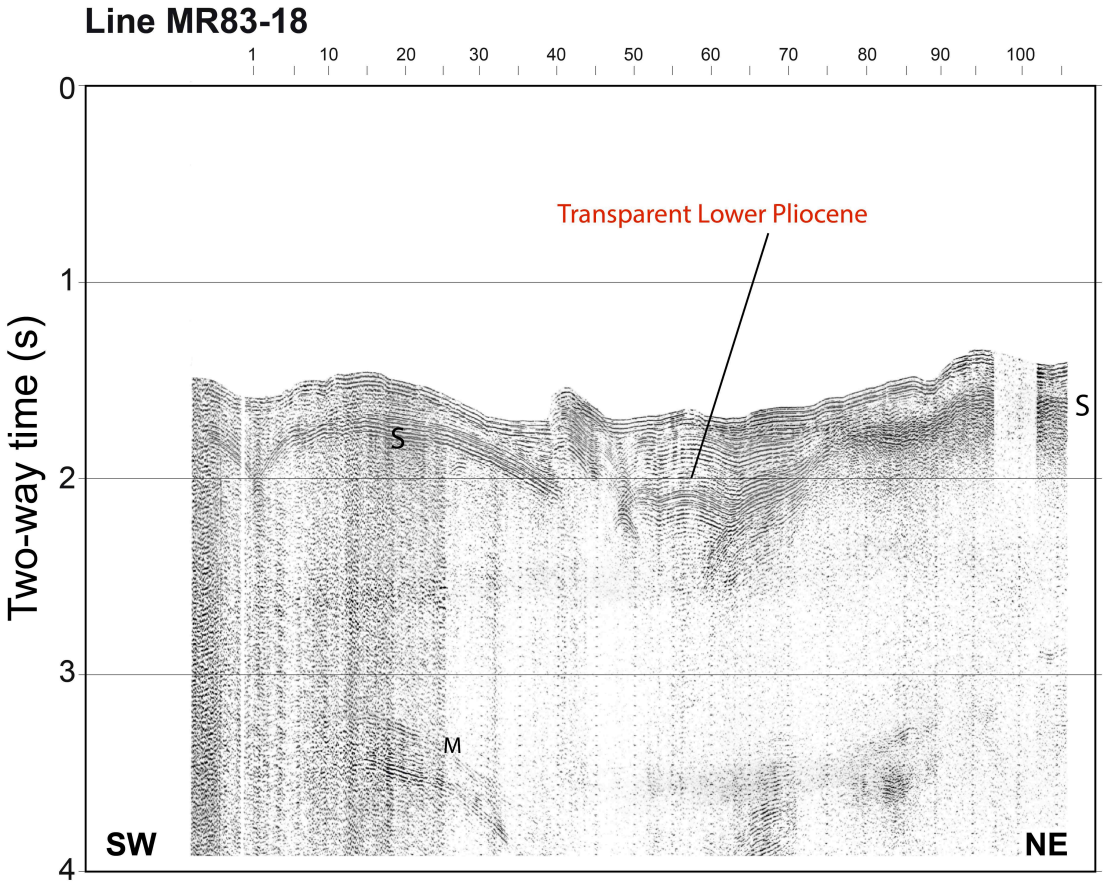

Figure ES1. Examples of seismic data collected on MV *Bannock* (cruise MR83 (Bonatti *et al.*, 1984)) located in Figure 5 showing the character of the S reflection and overlying PP sediments in the northern Red Sea.

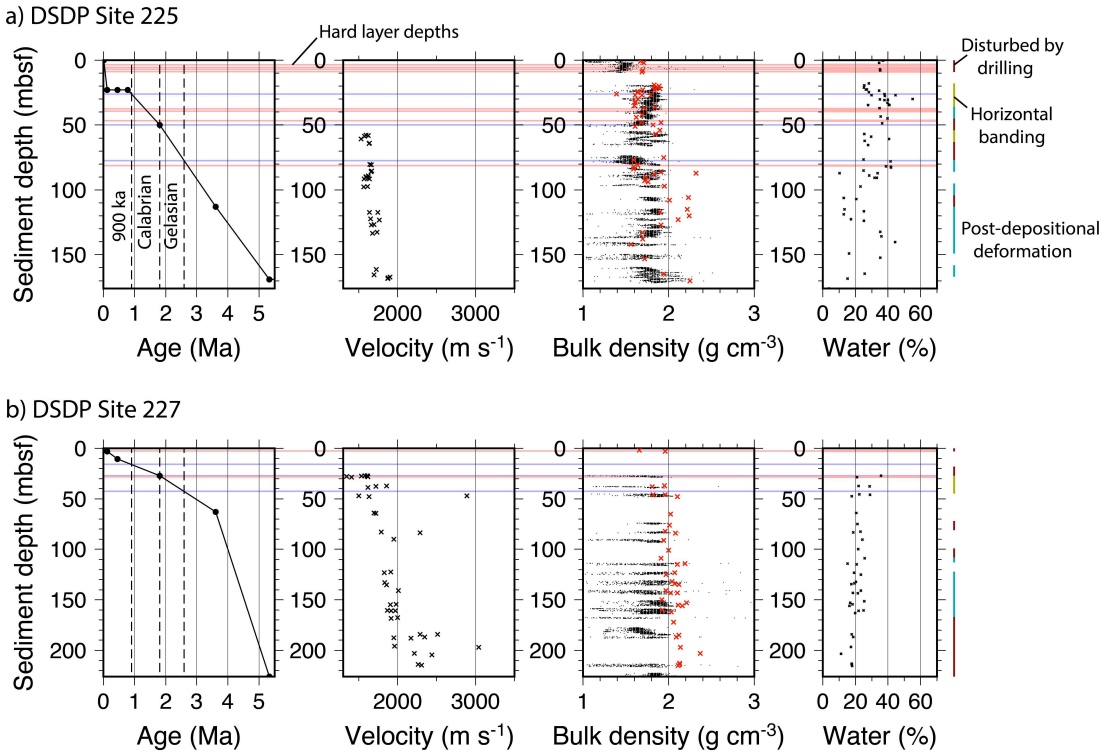

Figure ES2. Sediment property data for DSDP Sites (a) 225 and (b) 227 derived from the drilling reports (Whitmarsh *et al.*, 1974). Left graphs show the stratigraphic data updated to modern ages provided within the GeoMapApp database (WBF Ryan, pers. comm., 2009) (Gradstein & Ogg, 2004). Vertical dashed lines represent (from left to right) 900 ka (the first deep low-stand of sea level roughly marking the end of the Mid-Pleistocene Transition), and the onsets of the Calabrian and Gelasian stages. Horizontal blue lines show their corresponding sediment depths. Velocities in second graphs are the shipboard P-wave velocities measured on samples. Bulk densities in third set of graphs include the gamma ray attenuation porosity evaluator (GRAPE) values shown as fine points and (red) measurements on samples using a micropycnometer (Manheim *et al.*, 1974). The GRAPE measurements are noisy but their maximum values are similar to the sample measurements. Water contents in the final graphs are measurements of sediment water mass as a fraction of the solids

mass. Coloured bars on right represent segments of core interpreted as showing drilling disturbance (red), horizontal sedimentary banding (yellow) and post-depositional deformation (blue), from Girdler and Whitmarsh (1974). Light red lines crossing all panels represent the depths of hard layers identified by Stoffers and Ross (1974).

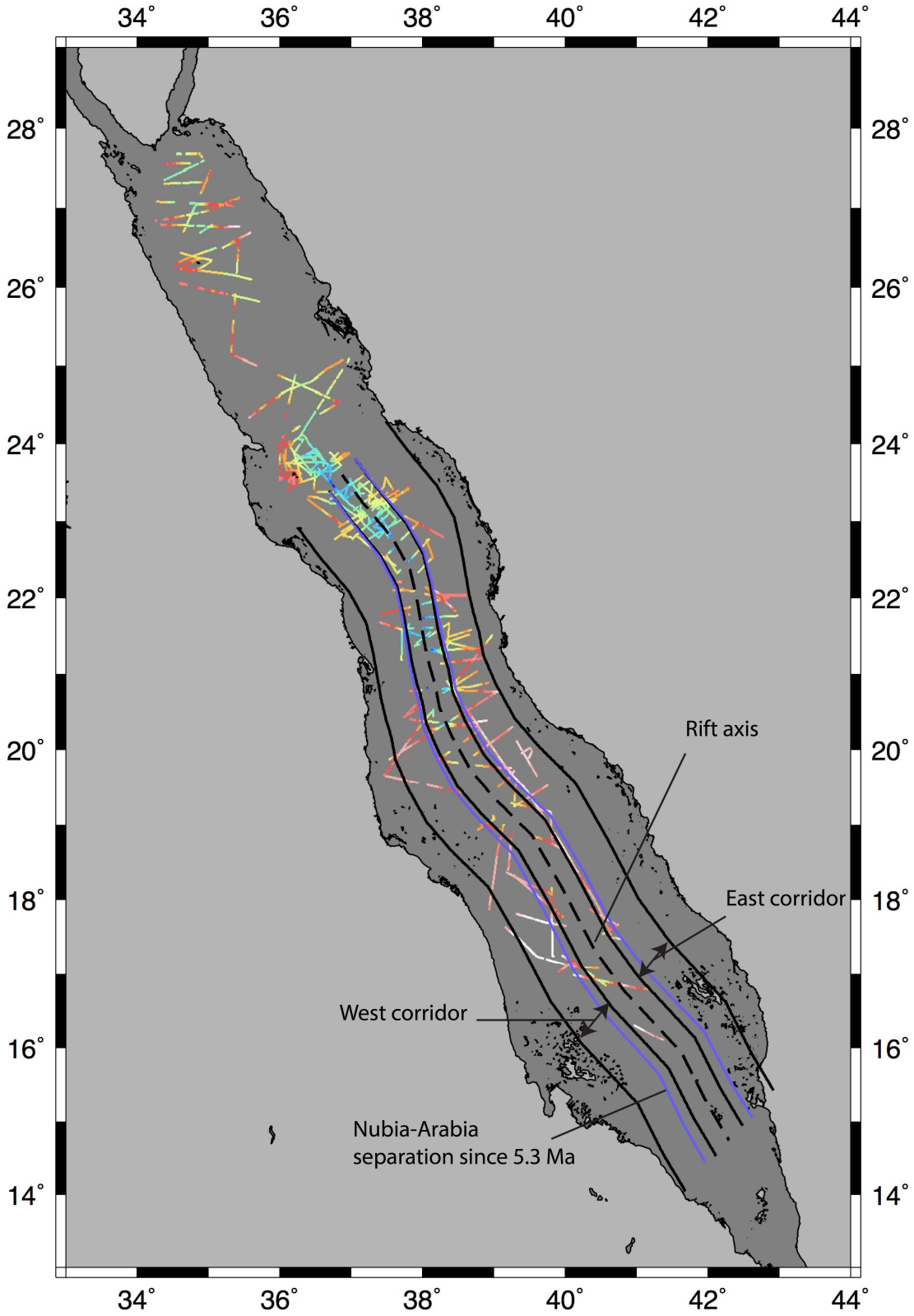

Figure ES3. Solid black lines mark corridors used to sample S-reflection depth and PP sediment thickness for the graphs in Figure 8. Corridors are 30 and 100 km from the spreading axis (dashed line). Blue lines represent the separation of

Nubia and Arabia since 5.3 Ma calculated using the rotation pole of Chu and Gordon (1998) assuming a constant rotation rate. Colours along ship tracks are S depths binned over 0.015˚ (colours as Figure 5a).

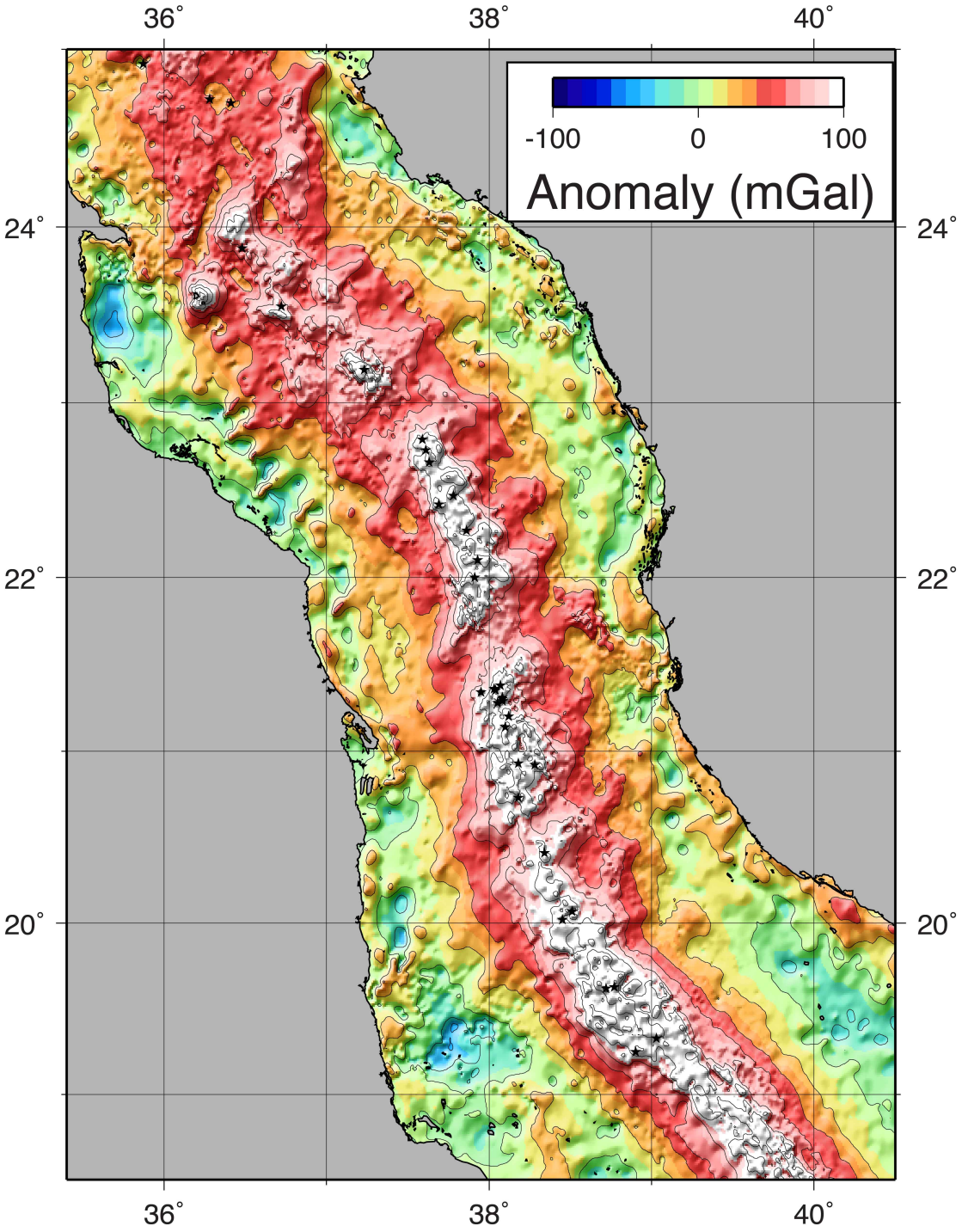

Figure ES4. Map of marine Bouguer anomalies obtained by correcting the free-air gravity field as in Figure 9b but using a density of 2.5 g cm^{-3} representing an average density of anhydrite and halite (Wheildon *et al.*, 1974). For comparisons between earlier versions of the free air anomalies of Sandwell and others and shipboard gravity anomalies, see Mitchell (2015) and Ligi et al. (2012). In particular, Mitchell (2015) found systematic patterns in maps of differences between the two measurement types, but they do not affect significantly the across-axis gravity depressions.

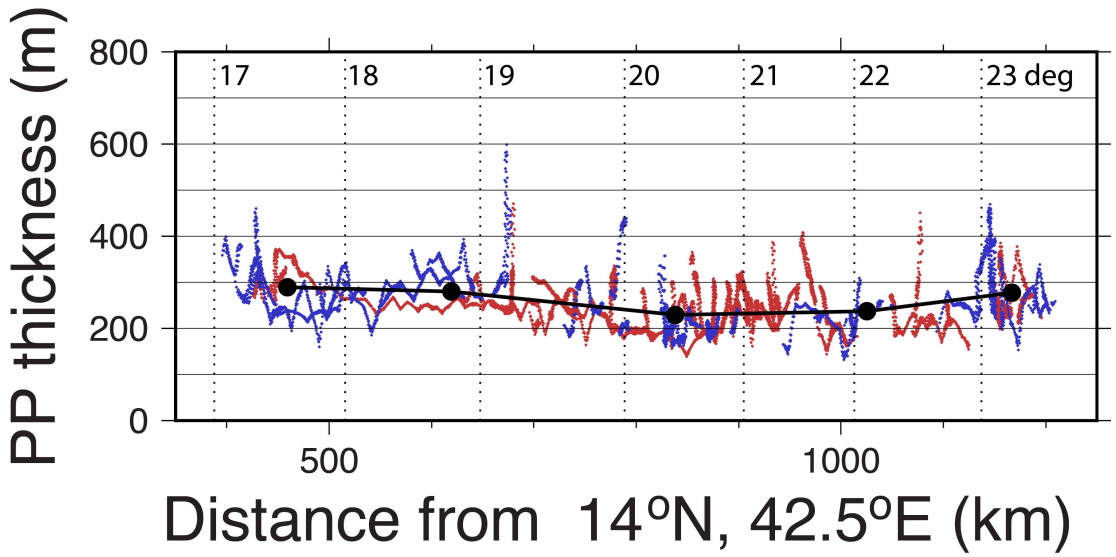

Figure ES5. Along-rift variations of thickness of Plio-Pleistocene sediments above S. Blue and red represent values from the west and east sides of the rift, respectively (Figure ES3). Black solid circles connected by solid lines are averages computed every 200 km (nominal 1σ standard errors of means are 1-2 m). Vertical dotted lines represent latitudes of the rift axis.